Journal of Vibration Engineering & Technologies (2026) 14:588
https://doi.org/10.1007/s42417-026-02823-y

ORIGINAL PAPER

Dimensionless Galerkin Benchmarks for Free Vibration of Longitudinally Graded Euler–Bernoulli Beams

Maryam Parvaresh[1] · **Elham Ghandi**[1] · **Shirin Esmaeili Niari**[1]

Received: 13 June 2026 / Revised: 19 September 2026 / Accepted: 8 October 2026
© Springer Nature Singapore Pte Ltd. 2026

Abstract

Purpose This study develops reproducible dimensionless Galerkin benchmarks for the axial and bending free vibration of prismatic longitudinally functionally graded Euler–Bernoulli beams under classical boundary conditions.

Methods Young's modulus and mass density are modeled as continuous power-law functions along the beam axis. Hamilton's principle is used to derive the variable-coefficient axial and transverse eigenvalue equations. A weak-form Galerkin formulation with Gauss–Legendre quadrature is then used to assemble dimensionless stiffness and mass matrices for axial and bending vibration.

Results The formulation is verified against exact homogeneous rod and Euler–Bernoulli beam solutions, published axially graded beam results, extended convergence and quadrature studies, and independent segmented Abaqus beam-element simulations. Relative to a 40-term bending reference, 10 Galerkin terms give a maximum selected-case bending error of 0.0152%, while 20 axial terms give a maximum error of 0.0016%. The maximum deviation from published axially graded beam data is 1.54%. The maximum Abaqus–Galerkin differences are 0.0202% for bending vibration and less than 0.006% for axial vibration. Increasing the power-law exponent from 0.1 to 10 reduces the first bending frequency by 44.26%, 40.85%, and 40.24% for SS, CC, and CF beams, respectively, and reduces the first axial frequency by 41.38%, 41.21%, and 42.18% for FF, FXFX, and FXF rods, respectively.

Conclusion The proposed dimensionless Galerkin formulation provides high-accuracy numerical benchmark frequencies for validating analytical, semi-analytical, and finite-element models of longitudinally graded slender beams within the stated Euler–Bernoulli scope.

Keywords Functionally graded beam · Longitudinal gradation · Galerkin method · Free vibration · Euler–Bernoulli beam theory · Dimensionless natural frequency

Introduction

Functionally graded materials (FGMs) are advanced composite materials whose physical and mechanical properties vary continuously in space [1]. Unlike laminated composites with sharp interfaces between layers, FGMs exhibit smooth variations in composition and properties, thereby reducing abrupt material discontinuities and the associated risks of interfacial stress concentration and delamination. It is for this reason that FGMs have become some of the most extensively used materials in aerospace engineering, thermal protection, nuclear power generation, biomedical applications, marine engineering, and mechanical engineering [2, 3]. The importance of the free vibration analysis of functionally graded beams (FGBs) is that natural frequencies and mode shapes characterize the dynamic response and help establish safe operating conditions for structures [4, 5]. Resonance can occur when an excitation frequency approaches a natural frequency, potentially producing large vibration amplitudes and structural damage [6]. More importantly, the dynamic behavior of beam-type systems is highly dependent on the beam theory used in modeling. The Euler–Bernoulli beam theory is well suited to slender beams because it assumes that cross-sections remain plane and normal to the neutral axis after deformation. Under the

✉ Elham Ghandi
ghandi@uma.ac.ir

[1] Department of Civil Engineering, Faculty of Technical and Engineering, University of Mohaghegh Ardabili, Ardabil, Iran

Published online: 20 October 2026

Euler–Bernoulli assumption, transverse shear deformation and rotary inertia are neglected, making the formulation most appropriate for slender beams and lower vibration modes. This yields a simple and efficient reference model. For moderately thick beams, however, Timoshenko beam theory is generally more appropriate because it accounts for transverse shear deformation and rotary inertia [7].

Recent studies conducted to understand the vibrational behavior of FGBs have focused on improving the efficiency of analysis through the consideration of the distribution of the material, porosity, boundary condition, theory of beams, elastic foundation, temperature, and numerical solutions. As the vibrational performance of FGBs is largely dependent upon the stiffness-inertia coupling phenomena, the type of material as well as the solution technique plays an important role in their vibrational response.

In this regard, Turan et al. [8] investigated porous FGBs using three different approaches, including analytical, finite-element, and artificial neural network methods, and found that the effects of the porosity distribution pattern, the power-law exponent, and the type of boundary conditions are significant for natural frequency and critical buckling load values. Additionally, Nguyen et al. [9] and Wu et al. [10] have emphasized the importance of shear deformation effects and proper beam theories for analyzing porous beams, thick beams, and higher vibration modes. Several studies have also addressed axially or longitudinally graded beams. Abdi et al. [11] analyzed axially functionally graded tapered Timoshenko beams using isogeometric analysis and reported that both axial gradation and tapering influence vibration and buckling responses. Burlayenko et al. [12, 13] studied axially graded beams with non-uniform and curvilinearly tapered cross-sections and showed that one-dimensional beam models can provide efficient predictions for relatively simple configurations, whereas more complex geometries may require higher-dimensional modeling. Huang and Li [14], Hein and Feklistova [15], Shahba and Rajasekaran [16], and Cao et al. [17] also provided important reference results for axially graded beams with variable stiffness and mass distributions. Sharma and Singh [18] further examined a clamped–clamped axially functionally graded beam with power-law longitudinal gradation using Timoshenko theory and the generalized differential quadrature method, providing a recent prismatic shear-deformable comparison.

In recent years, further studies on FGBs have been carried out considering porosity effects, elastic foundation, thermal environment, multi-physics coupling, and data-driven prediction. Al Rjoub and Obeidat [19] investigated axially functionally graded porous beams with varying cross-sections, while Tran et al. [20] studied a nonlocal dynamic stiffness model for the vibration analysis of stepped FGM nanobeams resting on a Winkler elastic foundation. Özmen and Özhan [21] combined analytical, computational, and experimental approaches for FGBs, and Jia et al. [22] examined the effect of a viscoelastic foundation. Thermal and multi-field effects have also been considered in recent studies by Yan et al. [23] and Nguyen et al. [24].

Recent developments also demonstrate that the adopted structural theory and geometric complexity can materially affect predicted natural frequencies. Shear-deformation formulations for porous or moderately thick FGBs [9, 10], Timoshenko analyses of tapered axially graded beams [11–13], and nonlocal or thermo-mechanical models [20, 23, 24] extend the physics beyond the classical slender-beam setting. These developments are important, but their additional kinematics, size effects, foundations, thermal fields, or non-prismatic geometry also change the governing eigenproblem and, in many cases, the frequency normalization. They therefore provide essential context for the present study but are not always suitable as direct numerical benchmarks for the simpler prismatic Euler–Bernoulli problem considered here. A recent multi-theory study by Taima et al. [25] likewise showed that, for a uniform beam with $L/h = 20$, classical beam theory agrees well for the first mode but departs progressively from shear-deformable theories at higher modes, reinforcing the need to state the modal range of Euler–Bernoulli benchmarks carefully.

Recent graphene origami-enabled auxetic metamaterial beam studies provide a complementary perspective on the role of structural kinematics. Karami and Ghayesh [26] compared dynamic predictions using different shear-deformation theories, while their subsequent studies addressed geometrically imperfect third-order beam structures [27] and nonlinear dynamics of third-order beams using a Galerkin-based weighted-residual approach [28]. These works illustrate how richer kinematics, imperfections and nonlinearity extend the scope of beam modelling. They also show why the use of Galerkin discretization alone is not a novelty claim. The present study instead focuses on a unified dimensionless weak-form treatment and numerical verification of linear axial and bending vibration in prismatic longitudinally graded beams. The cited metamaterial models provide methodological context, but their different constitutive and kinematic assumptions preclude treating their reported results as direct validation data without establishing an equivalent limiting problem.

Thermal coupling and small-scale effects constitute another distinct direction in graded-beam dynamics. Abouelregal et al. [29] investigated thermomechanical waves in functionally graded viscoelastic nanobeams using an Atangana-Baleanu fractional heat-conduction model. Abouelregal and Tiwari [30] studied a nonlocal graded nanobeam subjected to thermal shock. More recently, Abouelregal and Alsaeed [31] considered initially stressed silicon microbeams

with a nonlocal dual-phase-lag thermoelastic model and exponential through-thickness material variation. These studies extend graded-beam analysis through thermal fields, memory effects, initial stress or nonlocality; however, their coupled responses and, in some cases, different gradation directions do not directly represent the purely mechanical longitudinally graded free-vibration problem treated here. Numerical comparison would require matched material profiles, boundary conditions and normalization, together with a justified reduction of the additional physics. They therefore motivate future multiphysics extensions while helping delineate the scope of the present classical benchmark.

Despite the considerable progress made in the vibration analysis of FGMs, two gaps remain important for verification-oriented studies. First, many published formulations emphasize thickness-wise gradation, porosity, tapering, foundations, thermal effects, or advanced structural theories, while longitudinally graded prismatic beams are often reported only for a single vibration family or support configuration. Second, compact dimensionless data sets that treat both rod-like axial motion and beam-like bending motion using the same longitudinal property law and normalization remain limited. A reproducible classical benchmark is therefore useful as a baseline against which more elaborate shear-deformable, non-prismatic, nonlocal, or multi-physics models can be checked.

A recent discrete physical model by Moukhliss et al. [32] also reports prismatic, foundation-free cases with purely longitudinal exponential gradation. These reduced cases provide a direct numerical comparison for the present Euler–Bernoulli formulation, complementing the model-level comparisons with shear-deformable and multiphysics studies.

To address these gaps, the present study establishes a compact and reproducible dimensionless benchmark for prismatic longitudinally graded Euler–Bernoulli beams. The contribution is not the Galerkin method itself; rather, it is the construction and systematic verification of a unified weak-form Galerkin framework for both axial and bending free vibration under several classical boundary conditions. The spatially varying Young's modulus and mass density are retained explicitly inside the stiffness and mass integrals instead of being replaced by equivalent homogeneous properties, and a common reference normalization is used across the axial and bending problems. The resulting frequency parameters are verified against exact homogeneous limiting solutions, directly compatible published axially graded beam results, extended convergence and quadrature studies, and independent Abaqus beam-element calculations. The final data are intended as reproducible high-accuracy numerical benchmark solutions for future analytical, semi-analytical, and finite element developments.

Mathematical Formulation

In this section, the mathematical modeling of the Galerkin-type solution of the free vibration problem of longitudinally functionally graded Euler–Bernoulli beams is presented. It is assumed that the material properties are spatially distributed following the power-law distribution. Hamilton's principle is used to obtain the governing axial and bending equations, and the resulting variable-coefficient eigenvalue equations are solved using a weak-form Galerkin approximation. The formulation is deliberately expressed in dimensionless form to make the final results suitable for benchmark comparison. Variational methods and Galerkin-type approximations have previously been used for vibrating systems with variable stiffness and mass characteristics [33, 34]. The present contribution is their systematic specialization and validation for prismatic longitudinally graded FGBs.

Material Gradation Model

A prismatic longitudinally graded FGB with a uniform rectangular cross-section is considered, as shown in Fig. 1. The beam has a length (L), width (b), thickness (h), and cross-sectional area ($A = bh$), and the second moment of area $I = bh^3/12$. In this coordinate system, which is right-handed, the x-axis is aligned with the beam axis, while the z-axis is measured relative to the centroidal axis of the section.

The effective material property $P(\xi)$, representing either Young's modulus $E(\xi)$ or mass density $\rho(\xi)$, is assumed to vary continuously along the axial direction according to a power-law distribution, which is commonly used in FGB formulations [14, 16] and [17]:

$$P(\xi) = P_L + (P_R - P_L)V(\xi) \tag{1}$$

where P_L and P_R denote the material properties at the left end $\xi = 0$ and the right end $\xi = 1$, respectively. The volume fraction of the right-end constituent is defined as:

$$V(\xi) = \left(\frac{x}{L}\right)^k = \xi^k, \ \xi = \frac{x}{L}, \ k > 0 \tag{2}$$

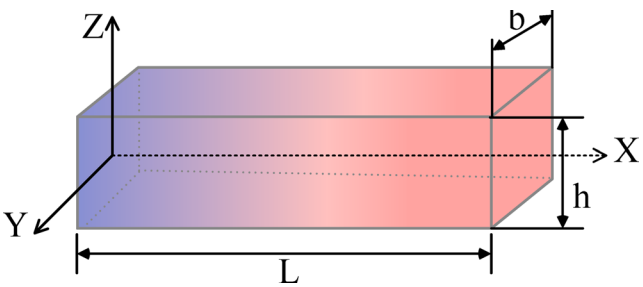


Fig. 1 Coordinate system and geometric notation for the longitudinally graded FGB

where k is the power-law exponent controlling the material distribution along the beam length. The case $k = 1$ represents a linear variation between the left-end and right-end constituents. Small values of k make the right-end constituent dominant over most of the span, while large values of k make the left-end constituent dominant, apart from regions near $\xi = 1$. In the limiting sense, as $k \to 0^+$, $V(\xi) = \xi^k$ approaches unity for $0 < \xi \leq 1$. Conversely, as $k \to \infty$, $V(\xi)$ approaches zero for $0 \leq \xi < 1$, while V(1) = 1 remains satisfied at the right end. The variation of the right-end constituent volume fraction $V(\xi)$ is illustrated in Fig. 2 against the normalized beam coordinate $\xi = x/L$ for different values of the power-law exponent k.

For a general longitudinally graded beam, the material at the left end and the material at the right end may be any two selected constituent materials. Therefore, Young's modulus and mass density are written as:

$$E(\xi) = E_L + (E_R - E_L)\,\xi^k \tag{3}$$

$$\rho(\xi) = \rho_L + (\rho_R - \rho_L)\,\xi^k \tag{4}$$

where E_L and ρ_L denote the Young's modulus and mass density of the material located at the left end ($\xi = 0$), while E_R and ρ_R denote the corresponding properties of the material located at the right end ($\xi = 1$). Power-law material distributions are widely used in FGB formulations because they provide a simple and controllable description of continuous property variation.

Kinematic Assumptions of Euler–Bernoulli Beam Theory

According to Euler–Bernoulli beam theory, plane cross-sections remain plane and normal to the deformed beam axis. Transverse shear deformation and rotary inertia are therefore neglected. This assumption is appropriate as a reference model for slender beams when these effects are secondary, but its physical accuracy generally deteriorates as the slenderness ratio decreases or the vibration mode order increases. The frequency parameters reported here should consequently be interpreted as Euler–Bernoulli benchmark solutions for slender prismatic beams, rather than as universal predictions for moderately thick beams or high-frequency regimes in which Timoshenko or higher-order shear-deformation theories are more appropriate.

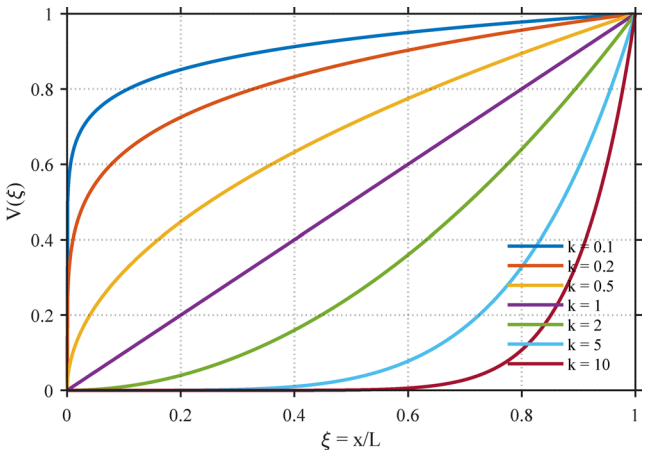


Fig. 2 Variation of the right-end constituent volume fraction $V(\xi)$ along the normalized beam coordinate

The displacement field of an arbitrary point of the beam is expressed as:

$$\begin{aligned} u_x(x,z,t) &= u_0(x,t) - z\frac{\partial w(x,t)}{\partial x} \\ u_z(x,z,t) &= w(x,t) \end{aligned} \tag{5}$$

where $u_0(x,t)$ is the axial displacement of the centroidal axis, $w(x,t)$ is the transverse displacement, z is the coordinate measured from the centroidal axis, and t is time.

The longitudinal normal strain is defined as:

$$\epsilon_x = \frac{\partial u_x}{\partial x} \tag{6}$$

Substituting Eq. (5) into Eq. (6) gives the following equation:

$$\epsilon_x = \frac{\partial u_0}{\partial x} - z\frac{\partial^2 w}{\partial x^2} \tag{7}$$

The normal stress is obtained from Hooke's law as:

$$\sigma_x = E(x)\epsilon_x \tag{8}$$

Since the material properties are uniform over each cross-section and vary only along the axial coordinate, and because the rectangular cross-section is symmetric, the centroidal and neutral axes coincide at each cross-section. Therefore, $\int_A z dA = 0$, and the axial–bending interaction term vanishes upon integration over the cross-section, so the two vibration problems can be solved separately.

Energy Expressions

The strain energy of the aforementioned beam [35] is written as follows:

$$U = \frac{1}{2}\int_0^L \int_A E(x) \left(\frac{\partial u_0}{\partial x} - z\frac{\partial^2 w}{\partial x^2}\right)^2 dA\,dx \tag{9}$$

Expanding the squared term gives:

$$U = \frac{1}{2}\int_0^L E(x)\begin{bmatrix}\left(\frac{\partial u_0}{\partial x}\right)^2 \int_A dA \\ -2\frac{\partial u_0}{\partial x}\frac{\partial^2 w}{\partial x^2}\int_A z\,dA \\ +\left(\frac{\partial^2 w}{\partial x^2}\right)^2 \int_A z^2\,dA\end{bmatrix} dx \tag{10}$$

$$\begin{aligned}&\int_A dA = A,\\ &\int_A z\,dA = 0,\\ &\int_A z^2\,dA = I\end{aligned} \tag{11}$$

Accordingly, the strain energy separates into axial and bending contributions:

$$U = U_a + U_b \tag{12}$$

where

$$U_a = \frac{1}{2}\int_0^L E(x)A\left(\frac{\partial u_0}{\partial x}\right)^2 dx \tag{13}$$

$$U_b = \frac{1}{2}\int_0^L E(x)I\left(\frac{\partial^2 w}{\partial x^2}\right)^2 dx \tag{14}$$

The kinetic energy is also decomposed as:

$$T = T_a + T_b \tag{15}$$

where

$$T_a = \frac{1}{2}\int_0^L \rho(x)A\left(\frac{\partial u_0}{\partial t}\right)^2 dx \tag{16}$$

$$T_b = \frac{1}{2}\int_0^L \rho(x)A\left(\frac{\partial w}{\partial t}\right)^2 dx \tag{17}$$

The rotary inertia term is not included because the Euler–Bernoulli beam theory is adopted.

Governing Equations of Motion

Hamilton's principle is applied to derive the governing equations of motion [35] as follows:

$$\delta\int_{t_1}^{t_2}(T-U)\,dt = 0 \tag{18}$$

Using Eqs. (10)–(15), the governing equation for axial vibration is obtained as:

$$\frac{\partial}{\partial x}\left[E(x)A\frac{\partial u_0}{\partial x}\right] - \rho(x)A\frac{\partial^2 u_0}{\partial t^2} = 0 \tag{19}$$

The governing equation for transverse bending vibration is defined as:

$$\frac{\partial^2}{\partial x^2}\left[E(x)I\frac{\partial^2 w}{\partial x^2}\right] + \rho(x)A\frac{\partial^2 w}{\partial t^2} = 0 \tag{20}$$

For free vibration, harmonic motion is assumed as:

$$u_0(x,t) = U(x)e^{i\omega t} \tag{21}$$

$$w(x,t) = W(x)e^{i\omega t} \tag{22}$$

where ω is the natural circular frequency. Substituting Eqs. (21) and (22) into Eqs. (19) and (20) gives the axial and bending eigenvalue equations as:

$$\frac{d}{dx}\left[E(x)A\frac{dU}{dx}\right] + \omega^2\rho(x)AU = 0 \tag{23}$$

$$\frac{d^2}{dx^2}\left[E(x)I\frac{d^2W}{dx^2}\right] - \omega^2\rho(x)AW = 0 \tag{24}$$

The axial force, bending moment, and shear force are defined as:

$$N(x) = E(x)A\frac{dU}{dx} \tag{25}$$

$$M(x) = E(x)I\frac{d^2W}{dx^2} \tag{26}$$

$$V(x) = \frac{d}{dx}\left[E(x)I\frac{d^2W}{dx^2}\right] \tag{27}$$

The sign convention adopted for the bending moment does not affect the imposed zero-moment boundary conditions.

Boundary Conditions

In the present formulation, axial and transverse bending vibrations are treated as two independent eigenvalue problems because the material gradation is assumed only along the beam axis and the cross-section is symmetric. This means that there are no axial-bending coupling terms after integration across the section, enabling separate boundary conditions to be specified for axial and bending vibrations. The boundary conditions are set up using classical Euler–Bernoulli theory for beams and rods [36].

For bending vibration [37], the primary displacement variable is the transverse displacement $W(x)$, and the corresponding rotation is $\theta(x) = dW/dx$. The bending moment and shear force are expressed as $M(x)$ and $V(x)$, respectively.

Accordingly, an SS end requires zero transverse displacement and zero bending moment. A clamped end requires zero transverse displacement and zero rotation. A free end requires zero bending moment and zero shear force. For axial vibration, the primary displacement variable is the axial displacement $U(x)$, and the axial force is expressed as $N(x)$.

A fixed axial end needs zero axial displacement, while a free axial end needs zero axial force. For the FF axial case [38], the rigid-body translational mode is included in the admissible approximation space to preserve the completeness of the displacement field. This zero-frequency rigid-body mode is retained during the assembly and solution of the generalized eigenvalue problem but is excluded from the reported non-zero natural frequencies, as commonly done in free-vibration eigenvalue analysis. The axial and bending boundary conditions considered in this study are summarized in Table 1.

Galerkin Approximation

In the Galerkin discretization, the continuous axial and bending eigenvalue problems are projected onto finite-dimensional approximation spaces spanned by kinematically admissible trial functions. Instead of seeking the exact displacement amplitudes in closed form, the axial displacement amplitude $U(x)$ and the transverse displacement amplitude $W(x)$ are represented by truncated series expansions. The admissible functions utilized in these expansions are selected such that the essential, or geometric, boundary conditions of each support configuration are satisfied a priori, while the corresponding natural boundary conditions are enforced through the weak form of the governing equations. The unknown coefficients of the series represent generalized coordinates associated with the contribution of each admissible function to the approximate displacement field. In this way, the original variable-coefficient differential eigenvalue problems are transformed into finite-dimensional algebraic generalized eigenvalue problems, which can be solved systematically for the dimensionless natural frequency parameters. Accordingly, the axial and bending displacement amplitudes are approximated as follows [39, 40]:

$$U(x) \approx \sum_{j=1}^{N_a} a_j \phi_j(x) \tag{28}$$

$$W(x) \approx \sum_{j=1}^{N_b} b_j \psi_j(x) \tag{29}$$

Table 1 Boundary conditions considered for bending and axial vibration analyses

Analysis type	Case label	Boundary condition	Essential boundary conditions	Natural boundary conditions/treatment
Bending vibration	SS	Simply supported beam	$W(0) = 0$, $W(L) = 0$	$M(0) = 0$, $M(L) = 0$, where $M(x) = E(x) I W''(x)$
Bending vibration	CC	Clamped–clamped beam	$W(0) = 0$, $W'(0) = 0$, $W(L) = 0$, $W'(L) = 0$	—
Bending vibration	CF	Cantilever beam	$W(0) = 0$, $W'(0) = 0$	$M(L) = 0$, $V(L) = 0$, where $V(x) = d/dx[E(x)I W''(x)]$
Axial vibration	FF	Free–free rod	—	$N(0) = 0$, $N(L) = 0$, where $N(x) = E(x) A U'(x)$. The rigid-body zero-frequency mode is removed after eigenvalue extraction.
Axial vibration	FXFX	Fixed–fixed rod	$U(0) = 0$, $U(L) = 0$	—
Axial vibration	FXF	Fixed–free rod	$U(0) = 0$	$N(L) = 0$, where $N(x) = E(x) A U'(x)$

where N_a and N_b are the numbers of Galerkin terms used for the axial and bending approximations, respectively. The coefficients a_j and b_j are unknown generalized coordinates, while $\phi_j(x)$ and $\psi_j(x)$ are the admissible functions for axial and bending vibrations, respectively.

The weighting functions in the Galerkin method are selected from the same admissible function spaces used for the approximation. Multiplying the governing differential equation by the corresponding weighting function and integrating over the beam length gives the weak form [41]. For the axial vibration problem, the weighting function is taken as:

$$v(x) = \phi_i(x), \quad i = 1,2,\ldots,N \tag{30}$$

and for the bending vibration problem, it is taken as:

$$v(x) = \psi_i(x), \quad i = 1,2,\ldots,N_b \tag{31}$$

This choice ensures that the residual of the governing differential equation is orthogonal to the approximation space. Consequently, the Galerkin stiffness and mass matrices are formulated consistently for the axial and bending vibration problems. The Galerkin method is applied to all types of boundary conditions investigated here, allowing a comparison of the obtained frequency parameters.

Axial Admissible Functions

The axial admissible functions are selected according to the classical longitudinal vibration modes of rods and the requirements of the Galerkin approximation. These functions are chosen to satisfy the essential boundary conditions directly, while the natural axial-force conditions are satisfied through the weak formulation or by the selected modal basis.

Although the weak forms are first written in terms of the physical coordinate x, the admissible functions are more conveniently expressed in terms of the normalized coordinate, defined as follows:

$$\xi = \frac{x}{L} \tag{32}$$

For the FF axial case [38], a constant rigid-body basis function is included:

$$\phi_0^{FF}(\xi) = 1 \tag{33}$$

The non-zero deformation modes are represented by cosine functions:

$$\phi_j^{FF}(\xi) = \cos(j\pi\xi), \quad j = 1,2,\ldots,N_a \tag{34}$$

Therefore, the FF axial displacement amplitude can be written as follows:

$$U^{FF}(\xi) = a_0 + \sum_{j=1}^{N_a} a_j \cos(j\pi\xi) \tag{35}$$

The FF basis includes the rigid-body translation mode, which produces a zero eigenvalue. This zero-frequency mode is retained during matrix assembly and removed from the reported non-zero axial frequencies after eigenvalue extraction.

For the FXFX and FXF axial cases, the coefficient vector contains only N generalized coordinates.

For the FXFX axial case, the admissible functionsare:

$$\phi_j^{\mathrm{FXFX}}(\xi) = \sin(j\pi\xi), \quad j = 1,2,\ldots,N_a \tag{36}$$

These functions satisfy the essential displacement conditions $U(0) = U(L) = 0$.

For the fixed–free axial case, the admissible functions are defined as:

$$\phi_j^{FXF}(\xi) = \sin\left[\frac{(2j-1)\pi\xi}{2}\right], \quad j = 1,2,\ldots,N_a \tag{37}$$

These functions satisfy the essential condition $U(0) = 0$ at the fixed end, while the free-end axial force condition is naturally enforced through the weak form.

Bending Admissible Functions

The bending admissible functions are selected from classical Euler–Bernoulli beam mode-shape functions, which satisfy the essential boundary conditions of the corresponding support cases [37, 42]. For the SS bending case, the admissible functions are:

$$\psi_j^{SS}(\xi) = \sin(j\pi\xi), \quad j = 1,2,\ldots,N_b \tag{38}$$

These functions satisfy $W(0) = W(L) = 0$ and $W''(0) = W''(L) = 0$.

For the CC bending case, the admissible functions are selected as the classical Euler–Bernoulli CC mode-shape functions, which are defined as:

$$\psi_j^{CC}(\xi) = \cosh(\beta_j \xi) - \cos(\beta_j \xi) - \eta_j^{CC} \left[\sinh(\beta_j \xi) - \sin(\beta_j \xi)\right] \tag{39}$$

where

$$\eta_j^{CC} = \frac{\cosh(\beta_j) - \cos(\beta_j)}{\sinh(\beta_j) - \sin(\beta_j)} \tag{40}$$

The constants β_j are the positive roots of Eq. (38):

$$\cosh(\beta_j)\cos(\beta_j) - 1 = 0 \tag{41}$$

For the CF bending case, the admissible functions are selected as the classical Euler–Bernoulli CF mode-shape functions:

$$\psi_j^{CF}(\xi) = \cosh(\beta_j \xi) - \cos(\beta_j \xi) - \eta_j^{CF} \left[\sinh(\beta_j \xi) - \sin(\beta_j \xi)\right] \tag{42}$$

where

$$\eta_j^{CF} = \frac{\cosh(\beta_j) + \cos(\beta_j)}{\sinh(\beta_j) + \sin(\beta_j)} \tag{43}$$

The constants β_j are the positive roots of Eq. (41):

$$\cosh(\beta_j)\cos(\beta_j) + 1 = 0 \tag{44}$$

Galerkin Formulation for Axial Vibration

The weak form of the axial eigenvalue equation is obtained by multiplying Eq. (23) by the weighting function, integrating over the beam length, and applying integration by parts.

This step is the axial part of the proposed Galerkin solution method: the continuously varying axial stiffness and mass density are retained inside the integral operators rather than approximated by an equivalent homogeneous property.

The axial eigenvalue equation in Eq. (23) is first considered in the physical coordinate x. Multiplying Eq. (23) by an admissible weighting function $v(x)$ and integrating over the beam length gives the following equation [35]:

$$\int_0^L v(x) \left[\frac{d}{dx}\left(E(x)AU'(x)\right) + \omega^2 \rho(x) AU(x)\right] dx = 0 \tag{45}$$

The first term is integrated by parts:

$$\int_0^L v(x) \frac{d}{dx}\left[E(x)AU'(x)\right] dx = \left[v(x)E(x)AU'(x)\right]_0^L - \int_0^L E(x)AU'(x)v'(x)\,dx \tag{46}$$

Since $N(x) = E(x)AU'(x)$, the boundary term is $[vN]_0^L$. This term vanishes after applying the axial boundary conditions. At a free axial end $N = 0$, while at a fixed axial end $v = 0$ because the displacement is prescribed. Therefore, the axial weak-form becomes.

The axial displacement amplitude and the weighting function are approximated as:

$$\int_0^L E(x)AU'(x)v'(x)\,dx = \omega^2 \int_0^L \rho(x) AU(x) v(x)\,dx \tag{47}$$

Substituting Eq. (48) into Eq. (47) yields:

$$U(x) = \sum_{j=1}^{N_a} a_j \phi_j(x), \quad v(x) = \phi_i(x) \tag{48}$$

$$\sum_{j=1}^{N_a} a_j \int_0^L E(x) A \phi_i'(x) \phi_j'(x)\,dx = \omega^2 \sum_{j=1}^{N_a} a_j \int_0^L \rho(x) A \phi_i(x) \phi_j(x)\,dx \tag{49}$$

For the derivation of the dimensionless frequency parameters, the physical coordinate x is mapped onto the normalized coordinate $\xi = x/L$. This transformation leads to the following differential relations:

$$\int_A dA = A, \quad \int_A z\,dA = 0, \quad \int_A z^2\,dA = I \tag{50}$$

The dimensional axial stiffness and mass matrix entries are then written as follows:

$$K_{ij}^a = \frac{A}{L} \int_0^1 E(\xi) \phi_i'(\xi) \phi_j'(\xi)\,d\xi \tag{51}$$

$$M_{ij}^a = AL \int_0^1 \rho(\xi) \phi_i(\xi) \phi_j(\xi)\,d\xi \tag{52}$$

To obtain a fully dimensionless eigenvalue problem, the material properties are normalized with respect to the left-end reference properties as follows:

$$\widehat{E}(\xi) = \frac{E(\xi)}{E_{ref}}, \quad \widehat{\rho}(\xi) = \frac{\rho(\xi)}{\rho_{ref}} \tag{53}$$

where $E_{\text{ref}} = E_L$ and $\rho_{\text{ref}} = \rho_L$. Substituting $E(\xi) = E_{\text{ref}}\hat{E}(\xi)$ and $\rho(\xi) = \rho_{\text{ref}}\hat{\rho}(\xi)$ into the axial stiffness and mass matrices gives:

$$K_{ij}^{a} = \frac{E_{\text{ref}}A}{L}{}'K_{ij}^{a} \tag{54}$$

$$M_{ij}^{a} = \rho_{\text{ref}}AL{}'M_{ij}^{a} \tag{55}$$

where the dimensionless axial stiffness and mass matrices are defined as:

$$\bar{K}_{ij}^{a} = \int_0^1 \hat{E}(\xi)\phi_i'(\xi)\phi_j'(\xi)\,d\xi \tag{56}$$

$$\bar{M}_{ij}^{a} = \int_0^1 \hat{\rho}(\xi)\phi_i(\xi)\phi_j(\xi)\,d\xi \tag{57}$$

Therefore, the dimensional axial eigenvalue problem [35, 36] is transformed into the following dimensionless generalized eigenvalue problem:

$$\bar{K}^{a}\,\mathrm{a} = \left(\Omega_i^{a}\right)^2 \bar{M}^{a}\,\mathrm{a} \tag{58}$$

where the dimensionless axial frequency parameter is defined as:

$$\Omega_i^{a} = \omega_i^{a} L\sqrt{\frac{\rho_{ref}}{E_{ref}}} \tag{59}$$

The axial Galerkin equation expressed in Eq. (53) is then solved as a generalized eigenvalue problem after the integration and assembly of the dimensionless axial stiffness and mass matrices [34]. The eigenvalues obtained are the dimensionless squared axial frequencies. In the FF axial problem, the rigid-body translation leads to an eigenvalue of zero or close to zero that is excluded from the list of nonzero dimensionless axial frequencies [38]. The procedure for solving the axial generalized eigenvalue problem, elimination of the rigid-body axial modes, and reconstruction of the axial modal shapes using the eigenvectors of the Galerkin equation are described in Appendix A.

Galerkin Formulation for Bending Vibration

The weak form of the bending eigenvalue equation is obtained by multiplying Eq. (24) by the weighting function $\upsilon(x)$, integrating over the beam length, and applying integration by parts [34].

$$\begin{aligned}&\int_0^L \upsilon(x)\frac{d^2}{dx^2}\left[E(x)IW''(x)\right]\\ &dx - \omega^2\int_0^L \rho(x)AW(x)\upsilon(x)\,dx = 0.\end{aligned} \tag{60}$$

Applying integration by parts twice to the first term gives Eq. (56) as follows:

$$\begin{aligned}&\int_0^L \upsilon(x)\frac{d^2}{dx^2}\left[E(x)IW''(x)\right]\\ &dx = \left[\upsilon(x)V(x)\right]_0^L - \left[\upsilon'(x)M(x)\right]_0^L\\ &\quad + \int_0^L E(x)IW''(x)\upsilon''(x)\,dx\end{aligned} \tag{61}$$

The boundary terms vanish after applying the corresponding bending boundary conditions. Thus, the bending weak-form is obtained as:

$$\begin{aligned}&\int_0^L E(x)IW''(x)\upsilon''(x)\,dx\\ &= \omega^2\int_0^L \rho(x)AW(x)\upsilon(x)\,dx\end{aligned} \tag{62}$$

Using the Galerkin expansions:

$$\begin{aligned}&W(x) = \sum_{j=1}^{N_b} b_j\psi_j(x),\\ &\upsilon(x) = \psi_i(x),\ i = 1,2,\ldots,N_b\end{aligned} \tag{63}$$

Substituting Eq. (58) into Eq. (57) gives Eq. (59) as follows:

$$\begin{aligned}&\sum_{j=1}^{N_b} b_j\int_0^L E(x)I\psi_i''(x)\psi_j''(x)\,dx\\ &= \omega^2\sum_{j=1}^{N_b} b_j\int_0^L \rho(x)A\psi_i(x)\psi_j(x)\,dx\end{aligned} \tag{64}$$

Using the coordinate transformation $\xi = x/L$, one has

$$dx = L\,d\xi,\quad \frac{d^2\psi_j}{dx^2} = \frac{1}{L^2}\frac{d^2\psi_j}{d\xi^2} \tag{65}$$

Therefore, the bending stiffness and mass matrix components can be rewritten in the dimensionless coordinate as:

$$K_{ij}^{b} = \frac{I}{L^3}\int_0^1 E(\xi)\psi_i''(\xi)\psi_j''(\xi)\,d\xi \tag{66}$$

$$M_{ij}^{b} = AL\int_0^1 \rho(\xi)\psi_i(\xi)\psi_j(\xi)\,d\xi \tag{67}$$

Using the normalized material properties introduced in Eq. (48), these matrices can be expressed as:

$$K_{ij}^{b} = \frac{E_{\mathrm{ref}} I}{L^3} {}^{,b}K_{ij} \tag{68}$$

$$M_{ij}^{b} = \rho_{\mathrm{ref}} A L {}^{,b}M_{ij} \tag{69}$$

where the dimensionless bending stiffness and mass matrices are defined as:

$$\bar{K}_{ij}^{b} = \int_0^1 \hat{E}(\xi)\psi_i''(\xi)\psi_j''(\xi)\, d\xi \tag{70}$$

$$\bar{M}_{ij}^{b} = \int_0^1 \hat{\rho}(\xi)\psi_i(\xi)\psi_j(\xi)\, d\xi \tag{71}$$

Consequently, the bending eigenvalue problem is transformed into the following dimensionless generalized eigenvalue problem:

$$\bar{K}^{b}\,\mathrm{b} = \left(\Omega_i^{b}\right)^2 \bar{M}^{b}\,\mathrm{b} \tag{72}$$

where the dimensionless bending frequency parameter is defined as:

$$\Omega_i^{b} = \omega_i^{b} L^2 \sqrt{\frac{\rho_{ref} A}{E_{ref} I}} \tag{73}$$

For a rectangular cross-section, $A = bh$ and $I = bh^3/12$. Hence, Eq. (68) can also be written as:

$$\Omega_i^{b} = \frac{\omega_i^{b} L^2}{h} \sqrt{\frac{12\rho_{ref}}{E_{ref}}} \tag{74}$$

Once the dimensionless bending stiffness and mass matrices have been numerically integrated and assembled, Eq. (67) is solved as a generalized eigenvalue problem [34]. The positive eigenvalues are the squared dimensionless bending frequency parameters; their square roots therefore give the dimensionless bending natural frequencies. Details of the bending eigenvalue solution and mode-shape reconstruction are provided in Appendix A.

Numerical Results and Discussion

This section presents the numerical results obtained from the proposed dimensionless Galerkin formulation. First, the reference beam geometry, material properties, power-law gradation parameters, and numerical settings are introduced. The formulation is then verified against exact homogeneous Euler–Bernoulli beam and rod solutions, followed by comparison with published results for longitudinally graded beams. Convergence with respect to the number of Galerkin terms and the sensitivity of the Gauss–Legendre quadrature order is subsequently examined to confirm the numerical stability of the solution. An independent Abaqus beam-element verification is also performed for both bending and axial vibration cases. Finally, the validated formulation is used to generate benchmark dimensionless frequency parameters for different boundary conditions and power-law exponents, and the effects of longitudinal material gradation on axial and bending vibration responses are discussed.

Beam Specifications

The reference problem examines a beam with variable characteristics along its length. It consists of a uniform rectangular cross-section, but Young's modulus and density follow the longitudinal power-law variation. The left end is steel-rich, and the right end is alumina-rich. Table 2 lists the geometric and material properties used for the illustrative final calculations. The steel properties at the left end are used as the reference values for nondimensionalization.

The selected material pair provides a clear longitudinal stiffness-to-mass contrast. Alumina has a higher Young's modulus and lower density than steel; therefore, smaller values of the power-law exponent, which increase the alumina-dominated portion of the span, are expected to produce higher dimensionless natural frequencies. The length-to-height ratio is 20, supporting the use of the Euler–Bernoulli model as a slender-beam reference. Nevertheless, the higher-mode values reported in this work remain Euler–Bernoulli benchmark quantities; when shear deformation or rotary inertia is non-negligible for a specific physical beam, a Timoshenko or higher-order model should be used. Poisson's ratio does not enter the Euler–Bernoulli Galerkin formulation; it is used only in the Abaqus beam-element model and in the representative Timoshenko sensitivity check reported in Table 3.

Although the Galerkin eigenvalue problem is expressed in dimensionless form, the reported bending frequency parameter follows the Euler–Bernoulli normalization $\Omega_b = \omega L^2 \sqrt{\rho_{ref} A/(E_{ref} I)}$. Therefore, the tabulated Ω_b values are independent of the absolute size for geometrically similar rectangular beams, while the selected $L/h = 20$ is used to ensure the validity of the Euler–Bernoulli assumption and to define the Abaqus verification model.

Table 2 Geometric and material properties of the longitudinally graded FGB

Parameter	Symbol	Value
Beam length	L	2 m
Beam width	b	0.1 m
Beam height	h	0.1 m
Length-to-height ratio	L/h	20
Cross-sectional area	$A = bh$	0.01 m²
Second moment of area	$I = bh^3/12$	$8.33 \times 10^{-6}\ m^4$
Young's modulus of steel, left end	$E_s = E_L$	210 GPa
Density of steel, left end	$\rho_s = \rho_L$	7800 kg/m³
Young's modulus of alumina, right end	$E_{Al} = E_R$	390 GPa
Density of alumina, right end	$\rho_{Al} = \rho_R$	3960 kg/m³
Poisson's ratio	ν	0.3
Power-law exponent	k	0.1, 0.2, 0.5, 1, 2, 5, 10
Number of Galerkin terms for axial vibration	N_a	20
Number of Galerkin terms for bending vibration	N_b	10
Number of Gauss points	n_g	300

Table 3 Representative Euler–Bernoulli–Timoshenko sensitivity comparison for the longitudinally graded beam at $L/h = 20$ and $k = 2$

BC	Mode	Euler–Bernoulli Galerkin Ω_b	Timoshenko Ω_b	Difference (%)
SS	1	11.7181	11.6698	0.4118
SS	3	108.6253	104.6908	3.6221
SS	5	302.5731	275.1693	9.0569
CC	1	27.0691	26.6064	1.7092
CC	3	147.7332	138.2758	6.4017
CC	5	365.7921	319.5969	12.6288
CF	1	4.3952	4.3861	0.2070
CF	3	75.7360	73.2082	3.3376
CF	5	245.5377	224.0757	8.7408

Homogeneous Analytical Verification

The first verification stage evaluates the proposed Galerkin formulation against classical exact solutions of homogeneous Euler–Bernoulli beams and rods. In this limiting case, Young's modulus and mass density are taken as constant along the beam length, while the same nondimensionalization procedure used for the longitudinally graded beam is retained. This comparison verifies the admissible functions, boundary-condition implementation, nondimensionalization, matrix assembly, and eigenvalue extraction procedure before applying the formulation to variable-coefficient graded beams.

The dimensionless bending frequency parameter is defined in Eq. (69). For a homogeneous Euler–Bernoulli beam, the dimensionless bending frequency parameter is: $\Omega_b = \beta_n^2$. In particular, for the SS beam $\beta_n = n\pi$, whereas for the CC and CF beams, the characteristic equations are $\cosh(\beta_n)\cos(\beta_n) = 1$, $\cosh(\beta_n)\cos(\beta_n) = -1$, respectively. Table 4 shows that the Galerkin results reproduce the classical frequencies to the reported precision, validating the homogeneous bending implementation.

Table 4 Validation of the Galerkin formulation for homogeneous Euler–Bernoulli bending vibration

Boundary	Mode	Present Galerkin	Classical solution [37]
SS	1	9.8696	9.8696
SS	2	39.4784	39.4784
SS	3	88.8264	88.8264
SS	4	157.9137	157.9137
SS	5	246.7401	246.7401
CC	1	22.3733	22.3733
CC	2	61.6728	61.6728
CC	3	120.9034	120.9034
CC	4	199.8594	199.8594
CC	5	298.5555	298.5555
CF	1	3.5160	3.5160
CF	2	22.0345	22.0345
CF	3	61.6972	61.6972
CF	4	120.9019	120.9019
CF	5	199.8595	199.8595

The classical solutions are obtained from the characteristic frequency equations and dimensionless wave numbers reported by Han et al. [37].

The axial formulation is also validated against exact longitudinal vibration solutions of homogeneous rods [43]. For the FF axial rod, the rigid-body translational mode is included in the approximation space and removed after solving the generalized eigenvalue problem. The non-zero axial frequency parameters are $\Omega_a = n\pi$ for the FF and FXFX cases and $\Omega_a = (2n-1)\pi/2$ for the FXF case [44]. As reported in Table 5, the computed axial frequency parameters show near machine-precision agreement with the exact rod solutions. These results confirm the correct implementation of the axial Galerkin formulation and support its use as the homogeneous limiting case of the longitudinally graded beam problem.

Table 5 Validation of the Galerkin formulation for homogeneous Euler–Bernoulli axial vibration

Axial boundary condition	Mode	Present Galerkin	Classical solution [44]
FF	1	3.1416	3.1416
FF	2	6.2832	6.2832
FF	3	9.4248	9.4248
FF	4	12.5664	12.5664
FF	5	15.7080	15.7080
FXFX	1	3.1416	3.1416
FXFX	2	6.2832	6.2832
FXFX	3	9.4248	9.4248
FXFX	4	12.5664	12.5664
FXFX	5	15.7080	15.7080
FXF	1	1.5708	1.5708
FXF	2	4.7124	4.7124
FXF	3	7.8540	7.8540
FXF	4	10.9956	10.9956
FXF	5	14.1372	14.1372

To quantify the sensitivity of the Euler–Bernoulli benchmark to shear deformation and rotary inertia, a representative Timoshenko-beam calculation was carried out for the same steel–alumina graded beam at $L/h = 20$ and $k = 2$ as shown in Table 3. The Timoshenko model retains transverse shear deformation and rotary inertia, uses Poisson's ratio $\nu = 0.3$ and the rectangular-section shear correction factor 5/6, and was discretized with 400 two-node beam elements using selective reduced integration for the shear term. The same longitudinal $E(x)$ and $\rho(x)$ distributions and the same SS, CC, and CF boundary conditions were used. A mesh-doubling check to 800 elements changed the first five reported dimensionless frequencies by at most 0.0155%. A separate homogeneous simply supported check reproduced the classical Timoshenko frequencies [20] with a maximum first-five-mode error of 0.0172% on the 400-element mesh.

The comparison shows that the Euler–Bernoulli and Timoshenko predictions remain close for the first bending mode: the differences are 0.41%, 1.71%, and 0.21% for the SS, CC, and CF cases, respectively. The discrepancy increases with mode order, reaching 9.06%, 12.63%, and 8.74% for the corresponding fifth modes. The Timoshenko frequencies are systematically lower because transverse shear flexibility reduces the effective bending stiffness while rotary inertia increases the effective dynamic inertia. Accordingly, the present dimensionless frequencies are most appropriate as lower-mode benchmarks for slender beams; for higher modes or lower slenderness ratios, a shear-deformable theory should be preferred.

Comparison with Published and Recent Longitudinally Graded Beam Studies

An additional literature-based comparison is performed using published axially graded Euler–Bernoulli beam results reported by Cao et al. [17] and Shahba et al. [45]. The corresponding results are shown in Table 6. This comparison case differs from the steel–alumina power-law beam considered in the main parametric study; therefore, it is used only as an additional literature-based comparison for beams with longitudinally varying stiffness and mass. In this published case, the beam is geometrically uniform, and the normalized longitudinal material functions are defined as $\widetilde{E}(\xi) = 1 + \xi$, $\widetilde{\rho}(\xi) = 1 + \xi + \xi^2$.

The present Galerkin results show very close agreement with Shahba et al. [45], with the maximum difference remaining below 0.02%. The differences relative to Cao et al. [17] remain below 1.54%. These differences are still acceptable for a literature-based benchmark comparison and may be related to differences in normalization, numerical implementation, or rounding of the published values. This comparison confirms that the proposed Galerkin formulation can reproduce published bending frequencies of Euler–Bernoulli beams with longitudinally varying stiffness and mass properties.

Tables 7 and 8 compare recent results using matched material profiles and frequency normalization. The Moukhliss comparison directly assesses the Euler–Bernoulli formulation. For the thick beam studied by Abdi et

Table 6 Additional validation using the published axially graded Euler–Bernoulli bending reference

Boundary condition	Mode	Present Galerkin ($\Omega_n^{(P)}$)	Cao et al. [17] ($\Omega_n^{(C)}$)	Shahba et al. [45] ($\Omega_n^{(Sh)}$)	Differences relative to Cao et al. [17]	Differences relative to Shahba et al. [45]
CF	1	2.4256	2.439	2.426	0.55	0.02
CF	2	18.6042	18.437	18.604	0.90	0.00
CF	3	55.1793	54.339	55.180	1.52	0.00
SS	1	9.0286	9.053	9.029	0.27	0.00
SS	2	36.3715	35.834	36.372	1.48	0.00
SS	3	81.7291	80.470	81.732	1.54	0.00
CC	1	20.4721	20.585	20.472	0.55	0.00
CC	2	56.5485	56.251	56.549	0.53	0.00
CC	3	110.9399	109.869	110.947	0.97	0.01

Table 7 Direct Euler–Bernoulli comparison with Moukhliss et al. [32], Table 6 (prismatic beam with exponential axial gradation, $n_x = 3$, $n_y = 0$; no foundation)

BC	Mode	Present Galerkin Ω_G	Published DPM Ω_{DPM}	Difference (%)
CF	1	2.8545	2.889	1.1956
CF	2	21.4949	21.502	0.0330
SS	1	10.3669	10.366	0.0083
SS	2	41.9681	41.954	0.0336
CC	1	24.9364	24.958	0.0867
CC	2	67.1041	67.132	0.0416

al. [11], an independent Timoshenko control checks the published frequencies, while the Euler–Bernoulli results quantify the effect of omitting shear deformation and rotary inertia. These comparisons serve different purposes and are not combined into a single numerical error measure.

The first recent comparison uses the discrete physical model (DPM) of Moukhliss et al. [32], published online on 23 December 2025 and assigned to the 2026 volume. Their Table 6 contains a prismatic, foundation-free, purely axially graded case. The matched exponential material profile used in the present calculation is $V(\xi) = \frac{\exp(3\xi)-1}{\exp(3)-1}$, $(\xi) = [70 + 130V(\xi)]$ GPa, $\rho(\xi) = [2702 + 2998V(\xi)]$ kg m^{-3}.

Both methods neglect transverse shear deformation and rotary inertia. The common dimensionless bending-frequency normalization is $\Omega = \omega L^2\sqrt{\frac{\rho_m A}{E_m I}}$, $E_m = 70$ GPa, $\rho_m = 2702$ kg m^{-3}. Thus, this is a direct Euler–Bernoulli comparison with longitudinal gradation rather than a comparison of unlike structural theories.

The present values in Table 7 are newly computed using the same Galerkin weak form as the power-law calculations, but with the exponential property functions given above. The production settings are $N_b = 40$, $n_g = 300$. The first two bending modes are compared for CF, SS, and CC supports. Increasing the basis to 60 terms and checking 600 Gauss points confirms the numerical stability of the selected results. The percentage difference relative to the published DPM value is defined as $\Delta_{\mathrm{DPM}}(\%) = 100\frac{|\Omega_G - \Omega_{\mathrm{DPM}}|}{\Omega_{\mathrm{DPM}}}$. The maximum difference is 1.1956% for the first CF mode; all other listed differences are below 0.087%. These differences measure agreement with the reported discrete-model data and should not be interpreted as Galerkin truncation error.

The second comparison uses the first-mode IGA results in Table 4 of Abdi et al. [11] for a uniform zirconia-to-aluminum beam. The matched longitudinal power-law material functions are

$$E(\xi) = \left[200 - 130\xi^{k}\right] \text{GPa},$$
$$\rho(\xi) = \left[5700 - 2998\xi^{k}\right] \text{kg m}^{-3},$$
$$k \in \{1, 2, 3\}$$

.The frequency parameter is normalized with the left-end zirconia reference properties:

$$\Omega = \omega L^2\sqrt{\frac{\rho_L A}{E_L I}}, \quad E_L = 200\,\text{GPa}, \quad \rho_L = 5700\,\text{kg m}^{-3}$$

$$\frac{h}{L} = \sqrt{0.12} \approx 0.34641, \quad \nu = 0.3, \quad \kappa = \frac{5}{6}$$

The printed thickness ratio therefore corresponds to a thick beam and is distinct from the h/L = 0.05 steel–alumina example in the main study. The published results use Timoshenko theory; ν is Poisson's ratio and κ is the rectangular-section shear correction factor. Accordingly, a separate 800-element Timoshenko finite-element control is used for a like-for-like numerical check; it is not presented as a Euler–Bernoulli solution. Its assembly and verification are described in Appendix B.

In Table 8, the 2%-difference columns are evaluated from the following explicit definitions:

$$\Delta_{\mathrm{EB-IGA}}(\%) = 100\frac{\Omega_{\mathrm{EB}} - \Omega_{\mathrm{IGA}}}{\Omega_{\mathrm{IGA}}},$$
$$\Delta_{\mathrm{FEM-IGA}}(\%) = 100\frac{|\Omega_T - \Omega_{\mathrm{IGA}}|}{\Omega_{\mathrm{IGA}}}.$$

Table 8 Comparison of the first three bending frequencies with Abdi et al. [11], Table 5: power-law zirconia-to-aluminum beam $\frac{h}{L} = \sqrt{0.12}$. The Timoshenko FEM is an independent control calculation

Mode	BC	Present EB Ω_{EB}	Timoshenko FEM Ω_T	Published IGA Ω_{IGA}	EB–IGA (%)	FEM–IGA (%)
1	CF	4.3098	3.8963	3.8963	10.61	0.0003
1	SS	9.3371	7.8459	7.8459	19.01	0.0003
1	CC	20.9450	12.9066	12.9065	62.28	0.0005
2	CF	4.2860	3.8828	3.8828	10.39	0.0010
2	SS	9.5761	7.9873	7.9873	19.89	0.0001
2	CC	20.6084	12.6873	12.6873	62.43	0.0003
3	CF	4.1816	3.7957	3.7957	10.17	0.0011
3	SS	9.6904	8.0645	8.0645	20.16	0.0003
3	CC	20.4721	12.6030	12.6029	62.44	0.0006

Here Ω_{EB} is the present Euler–Bernoulli result, Ω_T is the independent Timoshenko finite-element result, and Ω_{IGA} is the published isogeometric-analysis result. The independent Timoshenko control agrees with the published IGA frequencies within 0.0011% at the precision reported in the source. The EB values are higher by approximately 10.17–62.44%, demonstrating the substantial effect of shear flexibility and rotary inertia for this thick-beam case. These large differences are a model-scope limitation, not a measure of error in solving the Euler–Bernoulli eigenproblem. Thus, Table 7 supports the longitudinally graded Euler–Bernoulli benchmark, while Table 8 independently checks the shear-deformable control and quantifies where a classical beam prediction should not be used.

Convergence and Numerical Integration Study

A convergence study is performed to verify the numerical stability of the proposed Galerkin formulation for the longitudinally graded steel–alumina beam. Unlike the homogeneous verification, this study is conducted for the actual FGB with spatially varying Young's modulus and mass density. The three different representative values of the power-law exponent k are chosen as 0.1, 2, and 10 for alumina-dominant, intermediate, and steel-dominant material distributions, respectively. The analysis is performed on the first, third, and fifth vibration modes to understand convergence behavior.

The dimensionless bending frequencies were evaluated using $N_b = 5, 8, 10, 12, 14, 16$, and 20 Galerkin terms and compared with a 40-term reference solution ($N_b^{ref} = 40$). For axial vibration, the existing reference calculation with $N_a^{ref} = 30$ is retained. Convergence errors for the two vibration problems are computed separately; the bending error for the nth mode is defined as:

$$e_{b,n}^{N_b} = \left| \frac{\Omega_{b,n}^{N_b} - \Omega_{b,n}^{\mathrm{ref}}}{\Omega_{b,n}^{\mathrm{ref}}} \right| \times 100, \tag{75}$$

where the first quantity denotes the nth dimensionless bending frequency parameter obtained with N_b terms and the reference quantity is computed with $N_b^{ref} = 40$. Similarly, the axial convergence error is defined using $N_a^{ref} = 30$:

$$e_{a,n}^{N_a} = \left| \frac{\Omega_{a,n}^{N_a} - \Omega_{a,n}^{\mathrm{ref}}}{\Omega_{a,n}^{\mathrm{ref}}} \right| \times 100 \tag{76}$$

For the axial problem, the reference value is obtained with $N_a^{ref} = 30$. The maximum errors reported in Table 9 are the largest relative differences over all considered boundary conditions, power-law exponents $k = 0.1$, 2, and 10, and the selected vibration modes 1, 3, and 5.

Table 9 Maximum convergence error of the Galerkin solution for the longitudinally graded beam

Vibration type	Galerkin terms	Reference terms	Maximum error (%)	Critical case
Bending	$N_b = 5$	$N_b^{ref} = 40$	5.3152	CC, $k = 2$, mode 5
Bending	$N_b = 8$	$N_b^{ref} = 40$	0.0666	CC, $k = 10$, mode 5
Bending	$N_b = 10$	$N_b^{ref} = 40$	0.0152	CC, $k = 10$, mode 5
Bending	$N_b = 12$	$N_b^{ref} = 40$	0.0062	CF, $k = 0.1$, mode 5
Bending	$N_b = 14$	$N_b^{ref} = 40$	0.0046	CF, $k = 0.1$, mode 5
Bending	$N_b = 16$	$N_b^{ref} = 40$	0.0035	CF, $k = 0.1$, mode 5
Bending	$N_b = 20$	$N_b^{ref} = 40$	0.0021	CF, $k = 0.1$, mode 5
Axial	$N_a = 5$	$N_a^{ref} = 30$	9.6810	FF, $k = 2$, mode 5
Axial	$N_a = 10$	$N_a^{ref} = 30$	0.0121	FXFX, $k = 0.1$, mode 5
Axial	$N_a = 15$	$N_a^{ref} = 30$	0.0038	FXFX, $k = 0.1$, mode 5
Axial	$N_a = 20$	$N_a^{ref} = 30$	0.0016	FXFX, $k = 0.1$, mode 5

For the higher-order CC and CF basis functions, the hyperbolic combinations were evaluated in algebraically equivalent scaled form to avoid subtractive cancellation at large characteristic roots. This numerical stabilization does not alter the admissible approximation space or the Galerkin formulation.

The axial formulation converges rapidly when the trigonometric admissible functions are used. For bending vibration, the extended assessment shows that the maximum error decreases from 5.3152% for $N_b = 5$ to 0.0666% for $N_b = 8$, 0.0152% for $N_b = 10$, and 0.0021% for $N_b = 20$, relative to the 40-term reference. The CC case remains the most demanding at lower approximation orders, while the steep-gradient CF fifth mode becomes critical after the CC error has decayed. On this basis, $N_b = 10$ and $N_a = 20$ are retained for the final frequency tables as an accuracy–efficiency compromise.

The extended results in Table 9 provide a substantially stronger convergence check than the original 10-versus-12-term comparison. With $N_b = 10$, the maximum selected-case bending error is approximately 0.0152% relative to the 40-term reference, and increasing to $N_b = 20$ reduces it to approximately 0.0021%. The axial solution remains even less sensitive to truncation, with a maximum error of 0.0016% at $N_a = 20$ relative to $N_a^{ref} = 30$. These errors are sufficiently small for the benchmark frequency tables reported below.

To evaluate the accuracy of the numerical integration procedure used in assembling the stiffness and mass matrices, a Gauss–Legendre quadrature sensitivity analysis is conducted, as detailed in Appendix A. This analysis is especially relevant for small power-law exponents, such as $k = 0.1$, where the material properties exhibit a steep variation near one end of the beam. Several quadrature orders, namely $n_g = 40$, 80, 120, 200, 300, and 500, are considered. The result obtained with $n_g = 500$ is adopted as the reference solution.

The results in Table 10 show that the maximum integration error is already below 0.002% when 40 Gauss points are used. With 300 Gauss points, the maximum difference relative to the 500-point reference solution is approximately 5.69×10^{-5}%. The slight non-monotonic difference between 200 and 300 Gauss points is negligible and is most likely caused by floating-point round-off rather than integration inaccuracy. Therefore, $n_g = 300$ is adopted in the final calculations to ensure stable and accurate numerical integration for all material gradation indices.

Table 10 Gauss–Legendre quadrature sensitivity for the bending Galerkin formulation

Number of Gauss points	Maximum error relative to $n_g = 500$ (%)
40	0.0019
80	4.08×10^{-4}
120	3.75×10^{-4}
200	4.83×10^{-5}
300	5.69×10^{-5}
500	0.0000

Abaqus-Based Finite Element Verification

An independent finite-element cross-check is performed using segmented Abaqus beam-element models to verify the Galerkin predictions for the longitudinally graded beam. The purpose of this finite-element verification is to provide an additional numerical check of the proposed solution, rather than to replace the exact analytical verification of the homogeneous limiting cases. A three-dimensional wire-beam model is constructed using the same geometric and material parameters adopted in the Galerkin formulation. The beam length is 2.0 m, and both the width and height are 0.1 m. The left end is assumed to be steel-rich, whereas the right end is alumina-rich.

Variation of the modulus of elasticity and mass density across the length of the beam can be modeled by segmenting the beam into various material segments. For each segment, Young's modulus and mass density are evaluated at the segment centroid according to the adopted power-law distribution and assigned to the corresponding beam section. A segmentation convergence test is performed using five sets of longitudinal material samples comprising 25, 50, 100, 200, and 400. Because one B33 beam element is assigned to each material segment, this study also serves as a mesh-refinement check for the Abaqus beam model. To assess segmentation accuracy under the steepest material gradient considered, the convergence assessment is performed for $k = 0.1$ using the first bending frequency of the CF beam. As shown in Fig. 3, the frequency decreases from 37.903 Hz with 25 segments to 37.865 Hz with 400 segments. Relative to the 400-segment reference, the differences are 0.1004%,

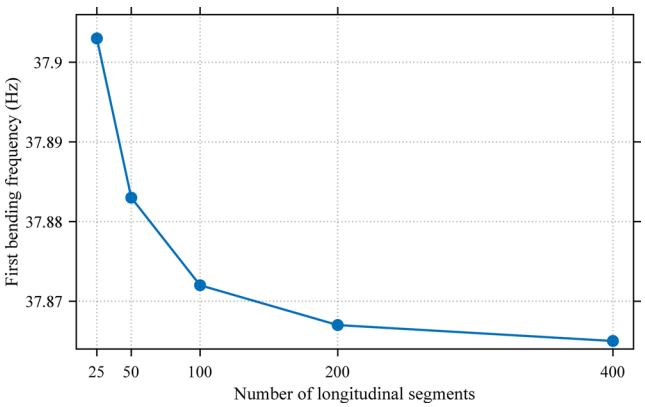


Fig. 3 Abaqus segmentation convergence for the first CF bending frequency at $k = 0.1$

0.0475%, 0.0185%, and 0.0053% for 25, 50, 100, and 200 segments, respectively. The corresponding 400-segment dimensionless frequency parameter is 6.353399, which agrees with the Galerkin value 6.3534 with a difference of approximately 1.6×10^{-5}%. These results demonstrate that the segmented Abaqus model remains sufficiently converged even for the steepest gradation case considered.

In the case of bending validation, the Abaqus model must be restricted to mimic the Euler–Bernoulli bending approach adopted in the Galerkin formulation. The out-of-plane displacement and rotations U_3, UR_1, and UR_2 are suppressed for all nodes, while U_1, U_2, and UR_3 remain active. For the SS beam, U_2 is constrained at both ends, and U_1 is constrained at the left end to remove axial rigid-body motion, while UR_3 remain free. For the clamped–clamped beam, U_1, U_2, and UR_3 are constrained at both ends. For the CF beam, U_1, U_2, and UR_3 are constrained at the left end, while the right end remains free. These settings reproduce the in-plane bending boundary conditions used in the Galerkin solution.

For axial validation, a separate axial-only Abaqus model is used. In this model, only the axial displacement degree of freedom U_1 is active, while transverse displacements and rotational degrees of freedom are suppressed. The same segmented longitudinal material representation is used. The first three axial frequencies are extracted for the FF, FXFX, and FXF axial boundary conditions. In the FF case, the zero-frequency rigid-body mode is removed before reporting the non-zero axial frequencies.

A linear perturbation frequency analysis with the Lanczos eigensolver is performed for each validation case. For bending vibration, the first three in-plane bending modes are identified by inspecting the mode shapes, because a three-dimensional beam model may also produce torsional or out-of-plane modes that are not directly comparable with the two-dimensional Euler–Bernoulli–Galerkin solution. Representative Abaqus mode shapes corresponding to the first three in-plane bending modes of the CF longitudinally graded beam are shown in Fig. 4. The extracted deformation patterns confirm that the selected modes are dominated by planar bending deformation and are therefore directly comparable with the Euler–Bernoulli–Galerkin formulation adopted in the present study.

The Abaqus frequencies in hertz are converted into dimensionless frequency parameters using the same reference modulus, reference density, beam length, and cross-sectional properties adopted in the Galerkin formulation. For bending vibration Ω_b is calculated as follows:

$$\Omega_{b,\mathrm{Abaqus}} = 2\pi f_{\mathrm{Abaqus}} L^2 \sqrt{\left(\frac{\rho_{\mathrm{ref}} A}{E_{\mathrm{ref}} I}\right)} \tag{77}$$

For the present reference properties and beam geometry, this relation gives $\Omega_b = 0.16779 f$, where f is expressed in hertz. For axial vibration, the corresponding dimensionless frequency parameter is:

$$\Omega_{a,Abaqus} = 2\pi f_{Abaqus} L \sqrt{\left(\frac{\rho_{ref}}{E_{ref}}\right)}. \tag{78}$$

For the present axial reference properties and beam length, this gives $\Omega_a = 0.00242185 f$. The percentage error is Error (%) $= |(\Omega_{Galerkin} - \Omega_{Abaqus})/\Omega_{Galerkin}| \times 100\%$. Three power-law exponents, $k = 0.5$, 2, and 10, are considered in both bending and axial finite element verifications. Since the wire-beam eigenvalue extraction may also return axial, torsional, or out-of-plane modes, only the in-plane bending-dominated modes are selected by inspecting the corresponding mode shapes.

Table 11 compares the first three dimensionless bending frequency parameters obtained from the Galerkin formulation with the corresponding Abaqus B33 beam-element results for different boundary conditions and power-law exponents. The maximum discrepancy is 0.0202%, which occurs for the third CF mode at $k = 0.5$. For all examined cases, the Abaqus–Galerkin differences remain below 0.021%, confirming the accuracy of the proposed Galerkin formulation and the consistency of the segmented finite-element validation model.

The axial validation results in Table 12 also show excellent agreement with the Galerkin formulation. For all considered power-law exponents, axial boundary conditions, and the first three axial modes, the differences remain below 0.006%. For the FF axial case, the zero-frequency rigid-body translational mode is present in the eigenvalue spectrum and is removed before reporting the first three non-zero axial frequencies.

In summary, the high correlation between the results obtained from the Galerkin method, segmented Abaqus beam element model, exact homogeneous solution, axially graded literature results, convergence analysis, and quadrature sensitivity analysis validates the correctness and repeatability of the proposed dimensionless approach for longitudinally graded Euler-Bernoulli beams.

Parametric Study

The final reference frequency parameters are computed using $N = 10$ Galerkin terms for bending vibration, $N = 20$ Galerkin terms for axial vibration, and $n_g = 300$ Gauss–Legendre quadrature points, as reported in Tables 13, 14, 15, 16, 17, 18 and 19. These numerical settings are selected based on the preceding convergence and quadrature studies.

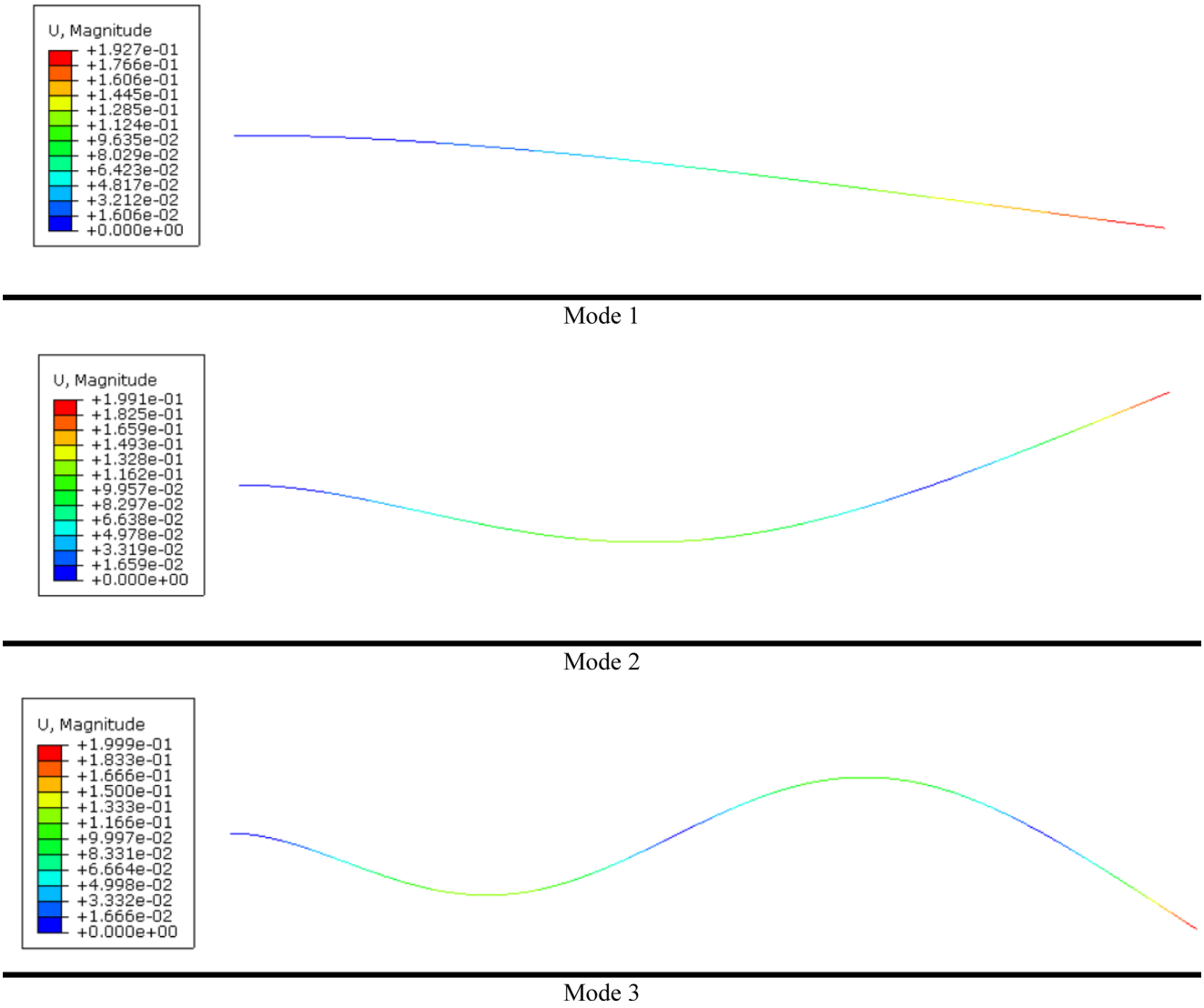


Fig. 4 First three in-plane bending mode shapes of the longitudinally graded CF beam obtained from the Abaqus B33 beam-element model

In the FF axial vibration problem, the constant rigid-body basis term is included in the approximation space and then discarded from the reported non-zero frequency set.

Table 13 presents the first five dimensionless bending frequency parameters for the SS beam. All frequency parameters decrease monotonically as the power-law exponent increases from 0.1 to 10. The first bending frequency decreases from 17.9168 to 9.9875, corresponding to a reduction of approximately 44.26%. These values form the SS bending part of the proposed reference dataset.

Table 14 reports the bending frequency parameters under CC boundary conditions. This support configuration produces the highest bending frequencies among the considered bending cases because both displacement and rotation are restrained at both ends. The first bending frequency decreases from 40.2475 at $k = 0.1$ to 23.8057 at $k = 10$.

Table 15 presents the bending frequency parameters for the CF beam. This configuration gives the lowest bending frequencies because one end is free, and the overall bending restraint is weaker than in the SS and CC cases. The first frequency decreases from 6.3534 at $k = 0.1$ to 3.7966 at $k = 10$.

Table 16 reports the first five non-zero dimensionless axial frequency parameters for the FF axial case. The rigid-body axial mode is excluded from the reported values. The first axial frequency decreases from 5.6211 at $k = 0.1$ to 3.2951 at $k = 10$.

Table 17 presents the axial frequency parameters under FXFX boundary conditions. Similar to the FF axial case, all frequency parameters decrease monotonically as k increases. The first axial frequency decreases from 5.6469 at $k = 0.1$ to 3.3197 at $k = 10$.

Table 11 Abaqus–Galerkin verification for the first three bending modes of the longitudinally graded FGB using B33 beam elements

BC	k	Mode	Abaqus f (Hz)	Abaqus Ω_b	Galerkin Ω_b	Difference (%)
SS	0.5	1	91.066	15.2821	15.2801	0.0131
SS	0.5	2	361.040	60.5856	60.5804	0.0086
SS	0.5	3	810.180	135.9535	135.9446	0.0065
SS	2	1	69.838	11.7182	11.7181	0.0009
SS	2	2	286.270	48.0355	48.0328	0.0056
SS	2	3	647.390	108.6317	108.6253	0.0059
SS	10	1	59.524	9.9874	9.9875	0.0010
SS	10	2	242.430	40.6787	40.6767	0.0049
SS	10	3	551.160	92.4876	92.4803	0.0079
CC	0.5	1	202.340	33.9544	33.9486	0.0171
CC	0.5	2	559.230	93.8391	93.8278	0.0120
CC	0.5	3	1097.400	184.1508	184.1175	0.0181
CC	2	1	161.320	27.0684	27.0691	0.0026
CC	2	2	447.640	75.1127	75.1100	0.0036
CC	2	3	880.450	147.7414	147.7332	0.0056
CC	10	1	141.870	23.8055	23.8057	0.0008
CC	10	2	387.470	65.0211	65.0183	0.0043
CC	10	3	758.280	127.2388	127.2447	0.0046
CF	0.5	1	32.184	5.4002	5.3997	0.0093
CF	0.5	2	201.450	33.7995	33.7996	0.0003
CF	0.5	3	561.740	94.2696	94.2506	0.0202
CF	2	1	26.194	4.3950	4.3952	0.0046
CF	2	2	160.430	26.9227	26.9186	0.0152
CF	2	3	451.360	75.7436	75.7360	0.0100
CF	10	1	22.626	3.7963	3.7966	0.0079
CF	10	2	138.790	23.2873	23.2895	0.0094
CF	10	3	387.270	64.9875	64.9863	0.0018

Table 18 presents the axial frequency parameters for the FXF case. These values are lower than those obtained for the FXFX and FF axial cases because one end is constrained in the axial direction while the other end is free, producing a quarter-wave deformation pattern. The first axial frequency decreases from 2.8456 at $k = 0.1$ to 1.6453 at $k = 10$.

Table 19 summarizes the reduction in the first dimensionless frequency parameter as k increases from 0.1 to 10. The reductions range from 40.24% to 44.26%, confirming that the longitudinal stiffness-to-density distribution has a major effect on both axial and bending vibration frequencies.

Among the analyzed cases, the SS bending case shows the largest reduction, indicating strong sensitivity of this mode to the longitudinal material distribution. The smallest reduction occurs for the CF bending case, suggesting that the boundary condition and modal deformation pattern influence how strongly the frequency parameter responds to the material gradient.

Because the results are expressed in dimensionless form, the frequency parameters in Tables 13, 14, 15, 16, 17, 18 and 19 should be interpreted as reference values for prismatic Euler–Bernoulli beams rather than dimensional frequencies for a single physical beam. The selected value of $L/h = 20$ is used to justify the slender-beam assumption and define the Abaqus verification model, while the dimensionless Galerkin frequency parameters remain independent of the absolute geometric scale within the present formulation.

Discussion

For the steel–alumina arrangement considered here, the dimensionless axial and bending frequency parameters decrease monotonically as the power-law exponent increases from 0.1 to 10. This trend should not be interpreted as a universal consequence of increasing the power-law exponent. When k is small, the right-end alumina constituent occupies a larger effective portion of the span; because alumina has both a higher Young's modulus and a lower density than steel, the mode-weighted stiffness-to-inertia ratio is increased. As k grows, the span becomes increasingly steel-dominated and the frequency parameters decrease. More fundamentally, the eigenfrequency depends on the simultaneous redistribution of stiffness and inertia: bending modes weight $E(x)$ through the curvature field and $\rho(x)$ through the displacement field, whereas axial modes weight $E(x)$ through axial strain and $\rho(x)$ through axial displacement. The resulting trend therefore depends on the

Table 12 Abaqus–Galerkin validation for axial vibration of the longitudinally graded FGB

Axial BC	k	Mode	Abaqus f (Hz)	Abaqus Ω_a	Galerkin Ω_a	Difference (%)
FF	0.5	1	1978.9	4.7926	4.7925	0.0021
FF	0.5	2	3941.4	9.5455	9.5450	0.0051
FF	0.5	3	5905.9	14.3032	14.3027	0.0036
FXFX	0.5	1	1953.8	4.7318	4.7316	0.0045
FXFX	0.5	2	3924.0	9.5033	9.5028	0.0057
FXFX	0.5	3	5892.0	14.2695	14.2688	0.0053
FXF	0.5	1	994.78	2.4092	2.4091	0.0045
FXF	0.5	2	2949.9	7.1442	7.1439	0.0045
FXF	0.5	3	4914.4	11.9019	11.9015	0.0038
FF	2	1	1589.2	3.8488	3.8489	0.0024
FF	2	2	3169.6	7.6763	7.6765	0.0026
FF	2	3	4747.7	11.4982	11.4983	0.0007
FXFX	2	1	1570.3	3.8030	3.8029	0.0035
FXFX	2	2	3149.7	7.6281	7.6281	0.0001
FXFX	2	3	4731.3	11.4585	11.4586	0.0008
FXF	2	1	785.48	1.9023	1.9023	0.0008
FXF	2	2	2380.3	5.7647	5.7648	0.0012
FXF	2	3	3958.7	9.5874	9.5874	0.0002
FF	10	1	1360.5	3.2949	3.2951	0.0052
FF	10	2	2728.8	6.6087	6.6088	0.0008
FF	10	3	4098.7	9.9264	9.9267	0.0026
FXFX	10	1	1370.7	3.3196	3.3197	0.0021
FXFX	10	2	2733.8	6.6209	6.6210	0.0021
FXFX	10	3	4095.1	9.9177	9.9179	0.0018
FXF	10	1	679.34	1.6453	1.6453	0.0024
FXF	10	2	2044.0	4.9503	4.9503	0.0007
FXF	10	3	3413.8	8.2677	8.2680	0.0034

Table 13 Dimensionless bending frequency parameters for the SS beam ($N = 10$)

Mode	$k = 0.1$	$k = 0.2$	$k = 0.5$	$k = 1$	$k = 2$	$k = 5$	$k = 10$
1	17.9168	17.1038	15.2801	13.4471	11.7181	10.3508	9.9875
2	71.2526	67.8144	60.5804	53.9121	48.0328	42.8552	40.6767
3	160.0043	152.1455	135.9446	121.3682	108.6253	97.3512	92.4803
4	284.1769	270.1095	241.3930	215.8090	193.4743	173.7355	165.2690
5	443.7741	421.7158	376.9401	337.2345	302.5731	271.9884	258.9786

Table 14 Dimensionless bending frequency parameters for the CC beam ($N = 10$)

Mode	$k = 0.1$	$k = 0.2$	$k = 0.5$	$k = 1$	$k = 2$	$k = 5$	$k = 10$
1	40.2475	38.1802	33.9486	30.2514	27.0691	24.5898	23.8057
2	110.8779	105.2338	93.8278	83.8396	75.1100	67.7185	65.0183
3	217.2597	206.2372	184.1175	164.7514	147.7332	132.9730	127.2447
4	359.0449	340.8709	304.5093	272.6530	244.6269	220.1114	210.3343
5	536.2584	509.1611	455.0234	407.5491	365.7921	329.1403	314.3203

Table 15 Dimensionless bending frequency parameters for the CF beam ($N = 10$)

Mode	$k = 0.1$	$k = 0.2$	$k = 0.5$	$k = 1$	$k = 2$	$k = 5$	$k = 10$
1	6.3534	6.0439	5.3997	4.8485	4.3952	3.9930	3.7966
2	39.7670	37.8247	33.7996	30.1831	26.9186	24.1850	23.2895
3	111.0240	105.4666	94.2506	84.4220	75.7360	68.0404	64.9863
4	217.3607	206.4308	184.5215	165.3678	148.5149	133.5859	127.3959
5	359.1489	341.0716	304.9308	273.3127	245.5377	221.0137	210.7612

Table 16 Dimensionless axial frequency parameters for the FF case ($N = 20$)

Mode	$k = 0.1$	$k = 0.2$	$k = 0.5$	$k = 1$	$k = 2$	$k = 5$	$k = 10$
1	5.6211	5.3386	4.7925	4.3021	3.8489	3.4484	3.2951
2	11.2568	10.6839	9.5450	8.5417	7.6765	6.9263	6.6088
3	16.8918	16.0279	14.3027	12.7922	11.4983	10.3904	9.9267
4	22.5264	21.3716	19.0621	17.0463	15.3209	13.8489	13.2413
5	28.1609	26.7150	23.8224	21.3020	19.1444	17.3056	16.5529

Table 17 Dimensionless axial frequency parameters for the FXFX axial case ($N = 20$)

Mode	$k = 0.1$	$k = 0.2$	$k = 0.5$	$k = 1$	$k = 2$	$k = 5$	$k = 10$
1	5.6469	5.3476	4.7316	4.2145	3.8029	3.4653	3.3197
2	11.2789	10.6877	9.5028	8.4920	7.6281	6.9009	6.6210
3	16.9116	16.0292	14.2688	12.7579	11.4586	10.3508	9.9179
4	22.5447	21.3713	19.0332	17.0203	15.2882	13.8063	13.2181
5	28.1780	26.7139	23.7969	21.2810	19.1168	17.2637	16.5214

Table 18 Dimensionless axial frequency parameters for the FXF axial case ($N = 20$)

Mode	$k = 0.1$	$k = 0.2$	$k = 0.5$	$k = 1$	$k = 2$	$k = 5$	$k = 10$
1	2.8456	2.7089	2.4091	2.1347	1.9023	1.7157	1.6453
2	8.4678	8.0276	7.1439	6.4001	5.7648	5.1892	4.9503
3	14.0982	13.3645	11.9015	10.6546	9.5874	8.6594	8.2680
4	19.7303	18.7047	16.6622	14.9107	13.4095	12.1200	11.5844
5	25.3630	24.0461	21.4237	19.1676	17.2326	15.5774	14.8974

Table 19 Summary of first dimensionless frequencies and reduction from $k = 0.1$ to $k = 10$

Vibration type	Boundary condition	Ω_1 at $k = 0.1$	Ω_1 at $k = 10$	Reduction (%)
Bending	SS	17.9168	9.9875	44.26
Bending	CC	40.2475	23.8057	40.85
Bending	CF	6.3534	3.7966	40.24
Axial	FF	5.6211	3.2951	41.38
Axial	FXFX	5.6469	3.3197	41.21
Axial	FXF	2.8456	1.6453	42.18

constituent property ratios, gradation direction, boundary conditions, mode shape, and nondimensionalization, and a different material pair or reversed gradation could produce a different trend.

The observed 40–44% change in the first dimensionless frequency is large enough to be relevant to engineering frequency placement. In a dimensional design, such a shift can substantially change the separation between a structural natural frequency and operating, aerodynamic, mechanical, or other excitation frequencies. Longitudinal gradation can therefore be used as a frequency-tuning variable, but it can also move a structure closer to resonance if the excitation spectrum is not considered. The dimensionless values reported here should consequently be converted using the actual geometry and reference material properties before resonance margins or safety factors are assessed for a specific aerospace, mechanical, or biomedical component.

Boundary conditions affect bending frequencies more strongly than axial frequencies. The CC case gives the highest bending frequency parameters because both displacement and rotation are restrained at both ends, increasing the bending strain energy. The CF beam produces the lowest values because one end remains free. For example, when $k = 2$, the first bending frequency parameters are 27.0691, 11.7181, and 4.3952 for the CC, SS, and CF beams, respectively.

For axial vibration, the FF and FXFX non-zero frequency parameters are very close, while the FXF values are substantially smaller. This is expected because the FF and FXFX rods have similar non-zero half-wave deformation patterns, whereas the FXF rod follows a quarter-wave pattern. For example, when $k = 2$, the first axial frequency parameters are 3.8489, 3.8029, and 1.9023 for the FF, FXFX, and FXF cases, respectively.

The mode-shape results are consistent with these interpretations. The first SS bending mode is symmetric and spans the full beam length. The CC mode reflects the stiffening effect of restrained displacement and rotation at both ends. The CF mode shows the expected maximum deflection at the free end. Therefore, the sensitivity of the dimensionless frequency parameter depends on the longitudinal material configuration as well as the mode shape.

The Abaqus verification further confirms the accuracy of the Galerkin solution. As shown in Table 11, the maximum discrepancy between the Abaqus B33 beam-element model and the Galerkin formulation is approximately 0.02% for the first three bending modes. This agreement indicates that the segmented finite-element representation correctly captures the same longitudinal stiffness and mass variation and that the Galerkin solution is consistent with classical Euler–Bernoulli beam modeling.

Figure 5 compares the first five dimensionless axial and bending frequency parameters for the longitudinally graded FGB at $k = 2$. The axial frequencies increase almost uniformly with mode order, and the FF and FXFX axial results remain close because their non-zero wavelength patterns are similar. In contrast, the bending frequencies differ more strongly among boundary conditions, showing the strong role of end rotational restraint and bending strain-energy distribution.

Figure 6 shows the normalized first bending mode shapes reconstructed from the Galerkin eigenvectors at $k = 2$. The SS mode satisfies the zero transverse displacement conditions at both ends and remains close to the classical sinusoidal profile, although the longitudinal variation of material properties may introduce slight asymmetry in the modal amplitude distribution. The CC mode satisfies zero displacement and rotation at both ends, whereas the CF mode exhibits the expected maximum bending displacement near the free end. The reconstructed Galerkin eigenmodes therefore satisfy the imposed boundary conditions and provide a physically consistent complement to the dimensionless frequency results.

To study the effect of material grading along the longitudinal direction of the beam independently of support configuration, the first modes of $k = 0.1,\ 2,$ and 10 cases have been normalized in Fig. 7. Despite the considerable changes in material distribution due to different k, the overall spatial distribution of the first bending mode does not change significantly. This suggests that the basic modal shape is

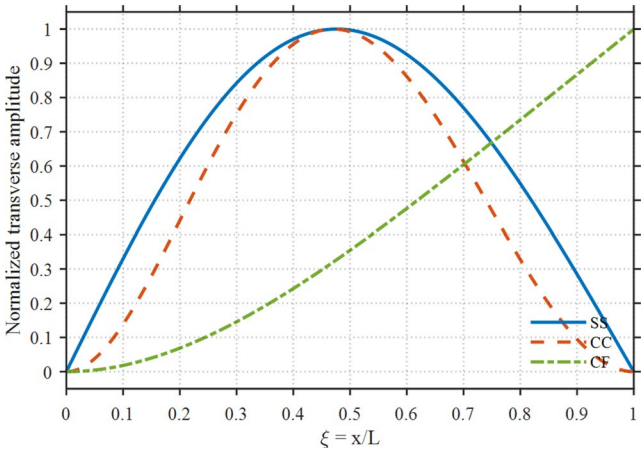


Fig. 6 Normalized first bending mode shapes of the longitudinally graded FGB reconstructed from Galerkin eigenvectors under SS, CC, and CF boundary conditions at $k = 2$

mostly determined by the applied boundary conditions, while longitudinal grading primarily modifies the stiffness and inertia distributions along the beam span. Accordingly, the observed changes in the normalized mode shapes are modest and mainly reflect shifts in the modal amplitude distribution.

Figure 8 shows the effect of the power-law exponent on the first dimensionless axial and bending frequency parameters. For the steel–alumina pair considered here, the reduction is steepest over the small-k range because changes in k strongly redistribute the alumina-rich portion of the span. As k increases, the beam becomes increasingly steel-dominated and the frequency curves gradually flatten. Thus, the power-law exponent acts as a control variable for the longitudinal stiffness-to-inertia distribution and, consequently, for the natural-frequency parameters.

The power-law model is deliberately adopted because it provides a simple one-parameter description of continuous longitudinal gradation and facilitates reproducible benchmark calculations. It does not represent all realizable material profiles. Exponential, sigmoid, piecewise-smooth,

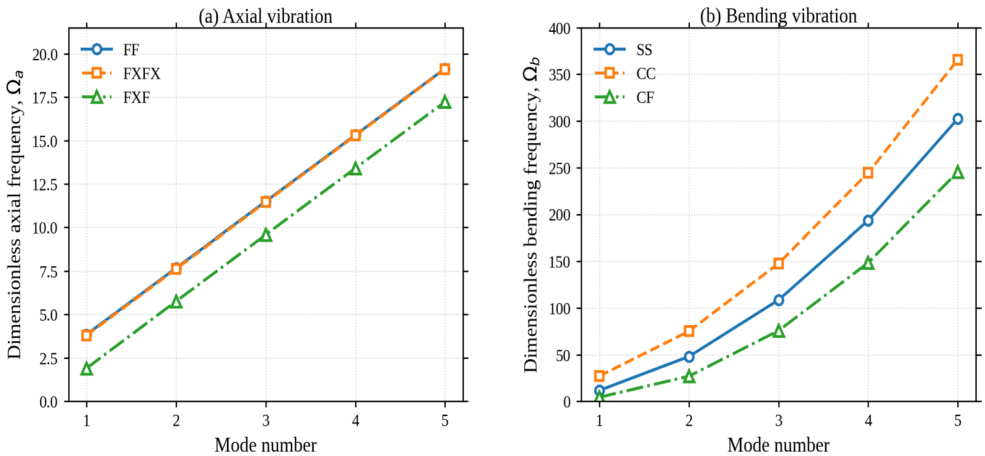


Fig. 5 Comparison of the first five dimensionless axial and bending natural frequencies of the longitudinally graded FGB under different boundary conditions at $k = 2$

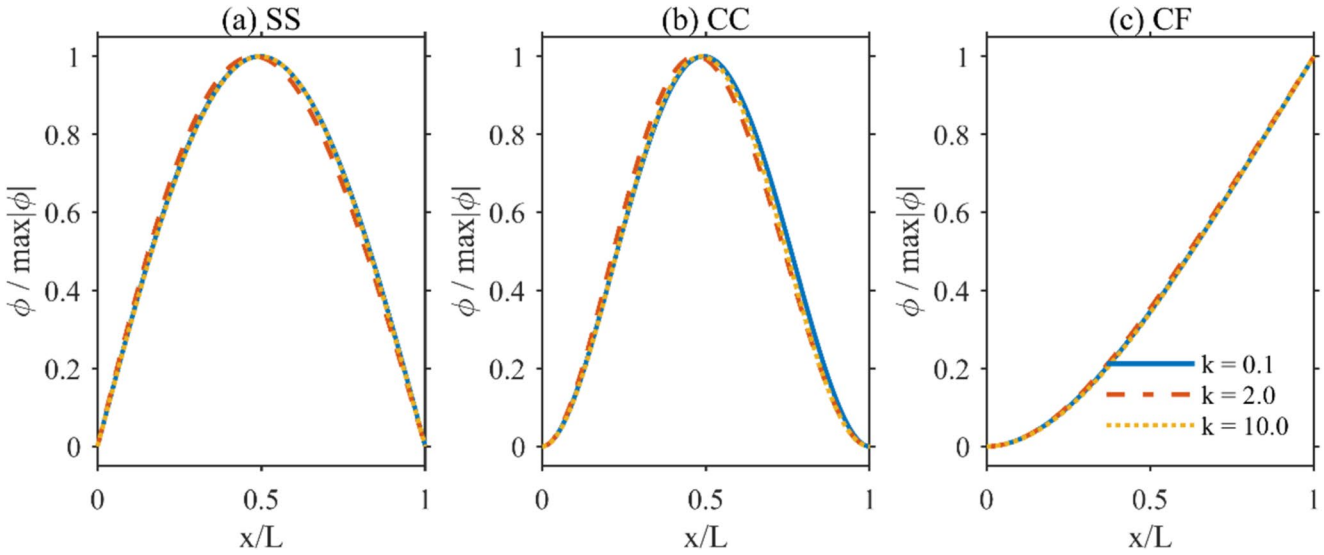


Fig. 7 Effect of longitudinal gradation on the normalized first bending mode shapes for SS, CC, and CF beams ($k = 0.1$, 2, and 10)

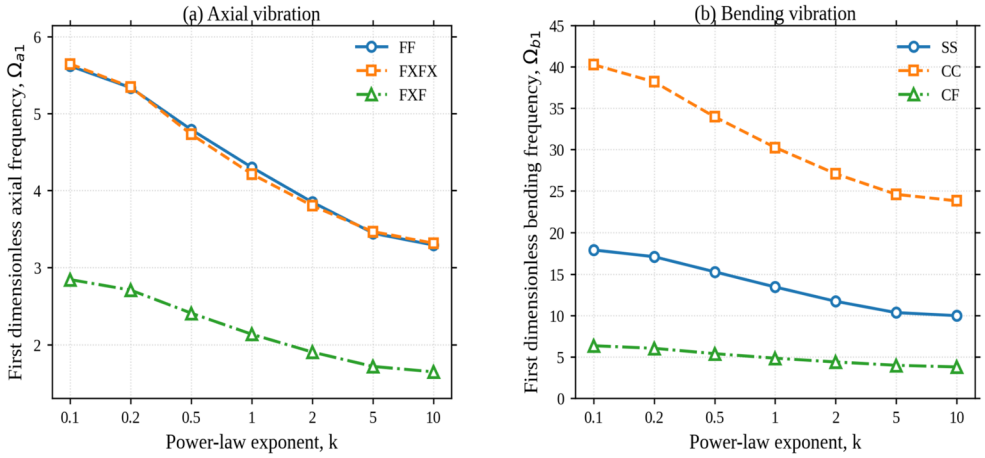


Fig. 8 Effect of the power-law exponent on the first dimensionless axial and bending natural frequencies of the longitudinally graded FGB under different boundary conditions

or experimentally measured gradation laws redistribute stiffness and inertia differently and may therefore produce quantitatively different, non-monotonic, or even opposite frequency trends. The present parametric conclusions are thus specific to the adopted power-law form and steel-to-alumina orientation.

The present weak-form framework can in principle be extended to non-prismatic or tapered beams by allowing the cross-sectional quantities $A(x)$ and $I(x)$ to vary spatially within the stiffness and mass integrals. Thermoelastic or nonlocal extensions would require additional constitutive, thermal, or length-scale terms and would therefore lead to modified governing operators and a separate validation procedure. Similarly, a Timoshenko or higher-order extension would introduce shear-deformation and rotary-inertia terms. These extensions are therefore feasible within the same variational/Galerkin philosophy, but they fall outside the scope of the present Euler–Bernoulli benchmark.

The verification strategy in this study is analytical and numerical. Exact homogeneous limiting solutions, published longitudinally graded results, convergence and quadrature checks, and independent Abaqus calculations provide complementary evidence of numerical accuracy, but experimental data for a beam manufactured with the same longitudinal steel–alumina profile and boundary conditions were not available. Experimental modal testing of purpose-built axially graded specimens is therefore an important next step for assessing manufacturing effects and the range of validity of the idealized material law.

Conclusion

This study developed a reproducible dimensionless weak-form Galerkin benchmark for the axial and bending free vibration of prismatic longitudinally functionally graded

Euler–Bernoulli beams. Young's modulus and mass density were allowed to vary continuously along the beam axis according to the same power-law description, and the two vibration families were formulated with a consistent reference normalization. Because the gradation is purely longitudinal and the rectangular cross-section is symmetric, axial and bending motions remain uncoupled within the adopted linear Euler–Bernoulli model.

Verification was carried out at several levels. The homogeneous limiting cases reproduced the classical exact rod and Euler–Bernoulli beam frequencies to machine precision. The literature-based bending comparison differed by at most 1.54% from Cao et al. [17] and by less than 0.02% from Shahba et al. [45]. The extended convergence study, using $N_b^{ref} = 40$, showed a maximum selected-case bending error of 0.0152% for $N_b = 10$ and 0.0021% for $N_b = 20$; the corresponding axial error for $N_a = 20$ relative to $N_a^{ref} = 30$ was 0.0016%. Gauss–Legendre integration was also stable, and the independent Abaqus comparison gave maximum Galerkin–Abaqus differences of 0.0202% for bending vibration and less than 0.006% for axial vibration. The representative Timoshenko sensitivity check at $L/h = 20$ and $k = 2$ showed first-mode differences of only 0.21–1.71%, whereas the fifth-mode differences increased to 8.74–12.63%, quantitatively confirming that the Euler–Bernoulli benchmark is most reliable for lower modes of slender beams. The graded-beam frequencies reported in this study should be interpreted as converged numerical benchmark results rather than analytical exact solutions.

The inclusion of the recently published literature comparisons provides separation between numerical verification and differences due to different structural theories. Comparison of the direct exponential AFG solution with Moukhliss et al. [32] gave 0.0083–1.1956% discrepancies for selected modes. For the case of the thick power-law AFG beam of Abdi et al. [11], the separate Timoshenko FEM control agreed with the published IGA results within 0.0011% at the reported precision, while Euler-Bernoulli predictions were 10.17–62.44% larger. Such a discrepancy highlights the necessity to match beam theory prior to assigning numerical validation errors.

For the assumed steel-to-alumina gradient, increasing the power-law exponent from 0.1 to 10 produced reductions of 44.26%, 40.85%, and 40.24% in the first bending frequency parameter for the SS, CC, and CF cases, respectively, and reductions of 41.38%, 41.21%, and 42.18% in the first axial frequency parameter for the FF, FXFX, and FXF cases, respectively. These reductions arise from the mode-specific redistribution of stiffness and inertia and depend on the selected materials and gradation direction; they should not be interpreted as a universal monotonic law. In terms of design, such deviations may influence frequency separations and resonance margins and make the longitudinal gradation a critical frequency tuning parameter.

Accordingly, the presented numerical results should be viewed as high-accuracy benchmarks rather than exact solutions. The present study is limited to linear free vibration of slender prismatic Euler–Bernoulli beams and rods with symmetric rectangular cross-sections and longitudinal power-law material gradation, and no directly matching experimental data are available. Future extensions should consider Timoshenko or higher-order shear-deformation models, alternative exponential or sigmoidal gradation laws, non-prismatic geometry, elastic foundations, damping, thermal and nonlocal effects, forced vibration, coupled multiphysics problems, and experimental modal testing of manufactured axially graded specimens.

Appendix A. Numerical Integration and Matrix Assembly

The stiffness and mass matrices in the present Galerkin formulation contain integrals with spatially varying coefficients. Since Young's modulus and mass density vary continuously along the normalized beam coordinate, closed-form evaluation of all matrix entries is not convenient for the general power-law material distribution and for all admissible functions. Therefore, Gauss–Legendre quadrature is employed to evaluate the dimensionless matrix integrals accurately and reproducibly.

For a general function $f(\xi)$, the Gauss–Legendre quadrature rule over the normalized interval is expressed as:

$$\int_0^1 f(\xi)\,d\xi \approx \sum_{g=1}^{n_g} w_g f(\xi_g) \tag{A.1}$$

where ξ_g and w_g are the Gauss point and its corresponding weight in the interval $[0,1]$, respectively, and n_g is the number of Gauss points.

For axial vibration, the dimensionless stiffness and mass matrix entries are evaluated as:

$$K_{ij}^{a} = \int_0^1 E(\xi)\phi_i'(\xi)\phi_j'(\xi)\,d\xi \approx \sum_{g=1}^{n_g} w_g E(\xi_g)\phi_i'(\xi_g)\phi_j'(\xi_g) \tag{A.2}$$

$$\begin{aligned} M_{ij}^{a} &= \int_0^1 \rho(\xi)\phi_i(\xi)\phi_j(\xi)\,d\xi \\ &\approx \sum_{g=1}^{n_g} w_g \rho(\xi_g)\phi_i(\xi_g)\phi_j(\xi_g) \end{aligned} \tag{A.3}$$

Similarly, for bending vibration, the dimensionless stiffness and mass matrix entries are computed as:

$$K_{ij}^{,b} = \int_0^1 E^{,}(\xi)\psi_i^{,,}(\xi)\psi_j^{,,}(\xi)d\xi \approx \sum_{g=1}^{n_g} w_g E^{,}(\xi_g)\psi_i^{,,}(\xi_g)\psi_j^{,,}(\xi_g) \tag{A.4}$$

$$M_{ij}^{,b} = \int_0^1 \rho^{,}(\xi)\psi_i(\xi)\psi_j(\xi)d\xi \approx \sum_{g=1}^{n_g} w_g \rho^{,}(\xi_g)\psi_i(\xi_g)\psi_j(\xi_g) \tag{A.5}$$

The quadrature procedure is implemented by looping over all Gauss points and accumulating the contribution of each point to every matrix entry. At each Gauss point, the normalized material properties $E^{,}(\xi_g)$ and $\rho^{,}(\xi_g)$ are first calculated from the power-law distribution. Then, the admissible functions and their required derivatives are evaluated at the same point. These values are multiplied by the corresponding Gauss weight and added to the appropriate stiffness or mass matrix entry.

The matrix assembly process may be summarized as follows:

For $g = 1,2,\ldots,n_g$:

evaluate $\xi_g,\ w_g,\ E^{,}(\xi_g),\ \rho^{,}(\xi_g)$,

evaluate $\phi_i(\xi_g)$, $\phi_i'(\xi_g)$,
$\psi_i(\xi_g)$, $\psi_i''(\xi_g)$,

assemble $K^{,a}$, $M^{,a}$, $K^{,b}$, $M^{,b}$.

After numerical integration, the assembled matrices are symmetrized to reduce numerical round-off errors:

$$\mathrm{K}^{,} \leftarrow \frac{1}{2}\left(\mathrm{K}^{,} + \mathrm{K}^{,T}\right), \tag{A.6}$$

$$\mathrm{M}^{,} \leftarrow \frac{1}{2}\left(\mathrm{M}^{,} + \mathrm{M}^{,T}\right). \tag{A.7}$$

This procedure preserves the continuously varying material distribution in the matrix formulation and avoids replacing the graded beam with an equivalent homogeneous model. In the present computations, Gauss points ($n_g = 300$) are used for the final results. The quadrature sensitivity study confirms that this value provides stable and sufficiently accurate matrix integration for all considered material gradation indices.

After numerical integration and matrix assembly, the dimensionless Galerkin systems for axial and bending vibrations are solved as generalized eigenvalue problems:

$$\mathrm{K}^{,a}\,\mathrm{a} = \lambda_a \mathrm{M}^{,a}\,\mathrm{a} \tag{A.8}$$

$$\mathrm{K}^{,b}\,\mathrm{b} = \lambda_b \mathrm{M}^{,b}\,\mathrm{b} \tag{A.9}$$

where a and b are the vectors of unknown Galerkin coefficients for axial and bending vibrations, respectively. The eigenvalues λ_a and λ_b correspond to the squared dimensionless frequency parameters:

$$\lambda_a = \Omega_a^2 \qquad \lambda_b = \Omega_b^2 \tag{A.10}$$

Hence, the dimensionless axial and bending frequency parameters are obtained by taking the square roots of the real positive eigenvalues. The computed eigenvalues are sorted in ascending order, and only physically meaningful positive values are retained. In the FF axial vibration case, the admissible function space includes a constant rigid-body translation term; consequently, a zero or near-zero eigenvalue appears in the spectrum. This eigenvalue represents rigid-body motion rather than deformational vibration and is therefore excluded from the reported non-zero axial frequency parameters.

The eigenvectors associated with the retained eigenvalues contain the Galerkin coefficients of the corresponding vibration modes. Thus, when mode-shape reconstruction is required, the axial and bending mode shapes are obtained by substituting the eigenvector components into the truncated series expansions of $U(\xi)$ and $W(\xi)$, respectively.

Appendix B. Implementation and Verification of the Added Recent-Literature Comparisons

The additional calculations in Tables 7 and 8 were executed in Python using NumPy and SciPy. The Euler–Bernoulli matrix assembly is a translation of the supplied MATLAB Galerkin implementation. For the CC and CF basis functions, the classical coefficients are.

$$\eta_j^{CC} = \frac{\cosh\beta_j - \cos\beta_j}{\sinh\beta_j - \sin\beta_j}, \qquad \eta_j^{CF} = \frac{\cosh\beta_j + \cos\beta_j}{\sinh\beta_j + \sin\beta_j} \tag{B.1}$$

Direct evaluation of $\cosh\beta_j$ and $\sinh\beta_j$ becomes poorly conditioned at high characteristic roots. To avoid forming $\delta_j = 1 - \eta_j$ by subtracting two nearly equal numbers, δ_j is evaluated from algebraically equivalent expressions containing only decaying exponentials and trigonometric terms:

$$\delta_j^{CC} = \frac{-2e^{-2\beta_j} + 2e^{-\beta_j}(\cos\beta_j - \sin\beta_j)}{1 - e^{-2\beta_j} - 2e^{-\beta_j}\sin\beta_j}$$
$$\delta_j^{CF} = \frac{-2e^{-2\beta_j} + 2e^{-\beta_j}(\sin\beta_j - \cos\beta_j)}{1 - e^{-2\beta_j} + 2e^{-\beta_j}\sin\beta_j} \quad \text{(B.2)}$$

For either support case, define.

$$t = \beta_j \xi\,,\ \delta_j = 1 - \eta_j,\ r_j = \delta_j e^{\beta_j} \quad \text{(B.3)}$$

$$H_j(t) = \cosh t - \eta_j \sinh t = \tfrac{1}{2}\left[r_j e^{t-\beta_j} + (2-\delta_j)e^{-t}\right] \quad \text{(B.4)}$$

Because $0 \le t \le \beta_j$, the factor $e^{t-\beta_j}$ never overflows, while r_j remains finite. This is algebraically identical to the classical admissible basis and only changes its numerical evaluation, thereby avoiding subtractive cancellation at high orders.

The Euler–Bernoulli comparison calculations use the following production discretization: $N_b = 40,\ n_g = 300$.

Across the selected comparisons, increasing the basis from 40 to 60 terms and, separately, increasing the quadrature from 300 to 600 Gauss points at 60 terms produce the following maximum relative frequency changes:

$$\max\left|\frac{\Delta\Omega}{\Omega}\right|_{N_b:40\to60} = 2.50\times10^{-5}\%,$$
$$\max\left|\frac{\Delta\Omega}{\Omega}\right|_{n_g:300\to600} = 1.06\times10^{-6}\% \quad \text{(B.5)}$$

The homogeneous first five bending modes provide an analytical check:

$$\max\left|\frac{\Omega_{\text{num}} - \Omega_{\text{exact}}}{\Omega_{\text{exact}}}\right| < 1.5\times10^{-8} \quad \text{(B.6)}$$

The original Cao material profile was also recalculated as a regression check. These checks apply to the new implementation and selected comparison cases; they do not replace the separate main-study convergence assessment.

For the independent Timoshenko control, transverse displacement w and cross-sectional rotation θ are interpolated independently with a linear two-node element. For an element of length ℓ_e, introduce the local coordinate and nodal vector.

$$s = \frac{x - x_e}{\ell_e} \in [0,1],\quad N_1 = 1 - s,\ N_2 = s,\quad \mathrm{q}_e = \begin{bmatrix} w_1 & \theta_1 & w_2 & \theta_2 \end{bmatrix}^T \quad \text{(B.7)}$$

$$w = N_1 w_1 + N_2 w_2,\quad \theta = N_1\theta_1 + N_2\theta_2,\quad G(x) = \frac{E(x)}{2(1+\nu)} \quad \text{(B.8)}$$

The element bending strain energy, shear strain energy, and kinetic energy are defined as:

$$U_b^{(e)} = \frac{1}{2}\int_{x_e}^{x_{e+1}} E(x) I\left(\theta'\right)^2 dx \quad \text{(B.9)}$$

$$U_s^{(e)} = \frac{1}{2}\int_{x_e}^{x_{e+1}} \kappa G(x) A(w' - \theta)^2 dx \quad \text{(B.10)}$$

$$T^{(e)} = \tfrac{1}{2}\int_{x_e}^{x_{e+1}} \rho(x) A\dot{w}^2 dx + \tfrac{1}{2}\int_{x_e}^{x_{e+1}} \rho(x) I\dot{\theta}^2 dx \quad \text{(B.11)}$$

With the nodal ordering in qe, define the interpolation and strain-displacement arrays $\mathrm{N}_w = \begin{bmatrix} N_1 & 0 & N_2 & 0 \end{bmatrix}$, $\mathrm{N}_\theta = \begin{bmatrix} 0 & N_1 & 0 & N_2 \end{bmatrix}$, $\mathrm{B}_b = \begin{bmatrix} 0 & N_1' & 0 & N_2' \end{bmatrix}$, $\mathrm{B}_s = \begin{bmatrix} N_1' & -N_1 & N_2' & -N_2 \end{bmatrix}$, so that the consistent element stiffness and mass matrices are assembled as:

$$\mathrm{K}_e = \int_{x_e}^{x_{e+1}} E(x) I\, \mathrm{B}_b^T \mathrm{B}_b dx + \int_{x_e}^{x_{e+1}} \kappa G(x) A\, \mathrm{B}_s^T \mathrm{B}_s\, dx \quad \text{(B.12)}$$

$$\mathrm{M}_e = \int_{x_e}^{x_{e+1}} \rho(x) A\, \mathrm{N}_w^T \mathrm{N}_w dx + \int_{x_e}^{x_{e+1}} \rho(x) I\, \mathrm{N}_\theta^T \mathrm{N}_\theta\, dx \quad \text{(B.13)}$$

Three-point Gauss integration is used for the bending and consistent mass terms, while one-point integration is used for the shear term to avoid locking. The longitudinal material functions E(x) and ρ(x) are evaluated at the integration points. After global assembly and application of the support constraints, the vibration problem is.

$$\mathrm{Kq} = \omega^2 \mathrm{Mq} \quad \text{(B.14)}$$

$$\Omega = \omega L^2\sqrt{\frac{\rho_L A}{E_L I}} \quad \text{(B.15)}$$

and the support conditions used for the comparison are

$$\mathrm{CF}:\ w(0) = 0,\ \theta(0) = 0;\ \mathrm{SS}:\ w(0) = w(L) = 0;\ \mathrm{CC}:\ w(0) = \theta(0) = w(L) = \theta(L) = 0$$

These constraints reproduce the CF, SS, and CC bending cases used in Table 8.

The 800-element control changes the selected first-mode results by at most 0.00092% relative to 400 elements. A homogeneous simply supported Timoshenko check, including the relevant shear/rotation branch when ordering the eigenvalues, agrees with the analytical first five frequencies within 0.00144%. Numerical comparisons use unrounded

computed values and the published reference precision. The calculation scripts, input parameters, comparison values, and convergence outputs are supplied as reproducibility material.

Author contributions Maryam Parvaresh carried out the mathematical formulation, numerical implementation, validation studies, data analysis, and prepared the first draft of the manuscript. Elham Ghandi supervised the research, guided the methodology, reviewed the results, and revised the manuscript critically. Shirin Esmaeili Niari advised the research, contributed to the interpretation of the results, and reviewed and revised the manuscript. All authors read and approved the final manuscript.

Funding The authors received no financial support for the research, authorship, and/or publication of this article.

Data Availability All data generated or analysed during this study are included in this article.

Declarations

Ethics Approval Not applicable.

Consent to Participate Not applicable.

Consent for Publication Not applicable.

Use of generative AI and AI-Assisted Technologies ChatGPT was used to improve readability, grammar, clarity, and consistency of the manuscript. The authors reviewed and edited the output and take full responsibility for the final content of the manuscript.

Competing interests The authors have no competing interests to declare that are relevant to the content of this article.

References

1. Boggarapu V et al (2021) State of the art in functionally graded materials. Compos Struct 262:113596
2. Kim K et al (2024) Free and forced vibration analysis of composite beam composed laminated composite material and functionally graded material. J Vib Eng Technol 12:7, 7349–7372
3. Pradhan P et al (2019) A state of the art in functionally graded materials and their analysis. Mater Today Proc 18:3931–3936
4. Celebi K, Tutuncu N (2014) Free vibration analysis of functionally graded beams using an exact plane elasticity approach. Proc Inst Mech Eng C J Mech Eng Sci 228(14):2488–2494
5. Lee JW, Lee JY (2017) Free vibration analysis of functionally graded Bernoulli-Euler beams using an exact transfer matrix expression. Int J Mech Sci 122:1–17
6. Zahedinejad P et al (2020) A comprehensive review on vibration analysis of functionally graded beams. Int J Struct Stab Dyn 20(04):2030002
7. Reddy JN et al (2021) Theories and analysis of functionally graded beams. Appl Sci 11(15):7159
8. Turan M et al (2023) Free vibration and buckling of functionally graded porous beams using analytical, finite element, and artificial neural network methods. Arch Appl Mech 93(4):1351–1372
9. Nguyen N-D et al (2022) A new two-variable shear deformation theory for bending, free vibration and buckling analysis of functionally graded porous beams. Compos Struct 282:115095
10. Wu S et al (2024) Examination of beam theories for buckling and free vibration of functionally graded porous beams. Materials (Basel) 17(13):3080
11. Abdi F et al (2025) Free vibration and buckling analysis of axially functionally graded tapered Timoshenko beams using B-spline-based isogeometric analysis. Heliyon 11:1
12. Burlayenko VN et al (2024) Free vibration analysis of curvilinearly tapered axially functionally graded material beams. Appl Sci (Basel) 14(15):6446
13. Burlayenko VN et al (2024) One-dimensional vs. three-dimensional models in free vibration analysis of axially functionally graded beams with non-uniform cross-sections. Mek Kompoz Mater 60(1):83–102
14. Huang Y, Li X-F (2010) A new approach for free vibration of axially functionally graded beams with non-uniform cross-section. J Sound Vib 329:11, 2291–2303
15. Hein H, Feklistova L (2011) Free vibrations of non-uniform and axially functionally graded beams using Haar wavelets. Eng Struct 33(12):3696–3701
16. Shahba A, Rajasekaran S (2012) Free vibration and stability of tapered Euler–Bernoulli beams made of axially functionally graded materials. Appl Math Model 36:7, 3094–3111
17. Cao D et al (2019) Free vibration of axially functionally graded beam. Mech Functionally Graded Mater Struct 1
18. Sharma P, Singh R (2021) A numerical study on free vibration analysis of axial FGM beam. Mater Today Proc 44:1664–1668
19. Al Rjoub YS, Obeidat HE (2026) Free vibration of axially functionally graded porous beams with varying cross-section. Int J Struct Stab Dyn 26(03):2550267
20. Tran LV et al (2023) Free vibration analysis of stepped FGM nanobeams using nonlocal dynamic stiffness model. J Low Freq Noise Vib Act Control 42(3):997–1017
21. Özmen U, Özhan BB (2025) Mechanics of functionally graded beams: analytical, computational, and experimental analyses. Int J Mech Mater Des 21:3, 577–590
22. Jia S et al (2025) Free vibration characteristics of functionally graded material (fgm) beams on three-parameter viscoelastic foundation. J Compos Sci 9(5):215
23. Yan Y et al (2024) Free vibration of functionally-graded piezoelectric semiconductor rectangular beam under thermal load. Phys B Condens Matter 690:416265
24. Nguyen T-N, Nguyen N-D (2025) A Ritz-type solution for free vibration and buckling analysis of functionally graded beams under hygro-thermal environment. In: Structures. p. 108392 Elsevier
25. Taima MS et al (2023) Comparative study on free vibration analysis of rotating bi-directional functionally graded beams using multiple beam theories with uncertainty considerations. Sci Rep 13:1, 17917
26. Karami B, Ghayesh MH (2024) Dynamics of graphene origami-enabled auxetic metamaterial beams via various shear deformation theories. Int J Eng Sci 203:104123
27. Karami B, Ghayesh MH (2025) Non-linear mechanics of geometrically imperfect graphene origami-enabled auxetic metamaterial third-order beam structures. Int J Non Linear Mech 172:105047
28. Karami B, Ghayesh MH (2026) Nonlinear dynamics of graphene origami enabled auxetic metamaterial third-order beams. Int J Non Linear Mech 105374
29. Abouelregal AE, Alsaeed SS (2026) Exploring the Vibrational Characteristics of Functionally Graded Silicon Microbeams Under Initial Stress Using a Novel Nonlocal Thermoelastic Framework. Silicon 18:7, 2631–2652

30. Abouelregal AE, Tiwari R (2024) Computational analysis of thermoelastic vibrations of functionally graded nonlocal nanobeam excited by thermal shock. J Vib Control 30:13–14
31. Abouelregal AE et al (2024) Coupled responses of thermomechanical waves in functionally graded viscoelastic nanobeams via thermoelastic heat conduction model including Atangana–Baleanu fractional derivative. Sci Rep 14(1):9122
32. Moukhliss A et al (2025) A discrete model for analyzing the free vibrations of a non-uniform 2D-FGM beam under elastic foundations and different support conditions. Sci Rep 16(1):2458
33. Alshorbagy AE et al (2011) Free vibration characteristics of a functionally graded beam by finite element method. Appl Math Model 35(1):412–425
34. Jin C, Wang X (2015) Accurate free vibration analysis of Euler functionally graded beams by the weak form quadrature element method. Compos Struct 125:41–50
35. Reddy JN (2017) Energy principles and variational methods in applied mechanics. John Wiley & Sons
36. Liu X et al (2022) Dynamic stiffness method for exact longitudinal free vibration of rods and trusses using simple and advanced theories. Appl Math Model 104:401–420
37. Han SM et al (1999) Dynamics of transversely vibrating beams using four engineering theories. J Sound Vib 225:5, 935–988
38. RD B (1984) Formulas for natural frequency and mode shape
39. Elishakoff I et al (2026) A Survey of Comparison Functions for Bernoulli-Euler Beams in Bending and Vibrations in Galerkin Method: 111 Years Later. Mech Res Commun 104716
40. Galerkin BG (1915) Series occurring in various questions concerning the elastic equilibrium of rods and plates. Eng Bull (Vestnik Inzhenerov) 19:897–908
41. Finlayson BA, Scriven LE (1966) The method of weighted residuals—a review. Appl Mech Rev 19:9, 735–748
42. Timoshenko S (1928) Vibration problems in engineering. van Nostrand
43. Meirovitch L (2010) Fundamentals of vibrations. Waveland Press
44. Rao SS, Yap FF (1995) Mechanical vibrations. Addison-Wesley, New York
45. Shahba A et al (2011) Free Vibration and Stability of Axially Functionally Graded Tapered Euler-Bernoulli Beams. Shock Vib 18:5, 683–696

Publisher's Note Springer Nature remains neutral with regard to jurisdictional claims in published maps and institutional affiliations.

Springer Nature or its licensor (e.g. a society or other partner) holds exclusive rights to this article under a publishing agreement with the author(s) or other rightsholder(s); author self-archiving of the accepted manuscript version of this article is solely governed by the terms of such publishing agreement and applicable law.